Thermal stability and oxidation processes in amphiboles on the tremolite – ferro-actinolite join studied by Raman spectroscopy

Bachelor Thesis

Mineralogisch-Petrographisches Institut
Universität Hamburg

Constanze Rösche

Supervised by:
Prof. Dr. Boriana Mihailova
Prof. Dr. Jochen Schlüter

Date of submission: 01.11.2018

Thermal stability and oxidation processes in amphiboles on the tremolite – ferro-actinolite join studied by Raman spectroscopy

Abstract

In this study an actinolite, the intermediate member of the tremolite – ferro-actinolite series, ideally $Ca_2(Mg,Fe^{2+})Si_8O_{22}(OH)_2$, has been examined regarding its thermal stability and oxidation behavior by conducting *in situ* Raman spectroscopic experiments. Spectra have been recorded in the ranges from 15-1215 cm^{-1} and 3370-3770 cm^{-1} at temperatures from 100-870 K in nitrogen atmosphere and at temperatures from room temperature to 1300 K in air. The heat treatment in nitrogen atmosphere did not cause any irreversible changes while on heating in air divalent iron is oxidized. At 1100 K hydrogen cations bonded to the oxygen anion at the W-site of the amphibole structure and electrons associated to Fe^{2+} at the octahedral sites start to delocalize but remain inside the crystal matrix. The delocalization is completed at 1300 K. When cooling to room temperature the initial state is only partly recovered. Therefore some hydrogen and electrons must have been ejected from the crystal. Changes in peak positions and intensities, new appearing and disappearing peaks indicate that some divalent iron has been oxidized to trivalent iron. In the final spectrum the peaks related to the chemical configurations $^{M(1)M(1)M(3)}Fe^{2+}MgMg–^{A}\square$ and $^{M(1)M(1)M(3)}Fe^{2+}MgMg–$A-site appear strongly shifted to lower wavenumbers with a decreased intensity, which indicates that the configurations have changed to $^{M(1)M(1)M(3)}Fe^{3+}MgMg–^{A}\square$ and $^{M(1)M(1)M(3)}Fe^{3+}MgMg–$A-site. New peaks have appeared at ~465 cm^{-1}, ~512 cm^{-1}, ~574 cm^{-1}, ~600 cm^{-1} and ~1170 cm^{-1}. Apart from slight changes in the SiO_4-ring and MO_6 octahedra geometry, which are due to the smaller size of Fe^{3+} as compared to Fe^{2+}, the structure of actinolite is preserved over the whole temperature range probed.

Table of contents

Figures

Tables

1 Introduction

Minerals belonging to the amphibole supergroup, which includes over 130 end-members and hypothetical compositions (Locock 2014), have aroused interest in the scientific community since the 18th century. At that time the designation amphibole did not exist and only few different species had been identified, but some minerals described in several mineralogical treaties match the characteristics. The name "amphibole" derives from the Greek word for "ambiguous" and was introduced in the 19th century by René J. Haüy because of two reasons: first because upon superficial examination amphiboles could be confused with tourmaline or pyroxene and second because the appearance of this minerals is often similar but the composition varies. Since then the chemical and physical properties of various amphiboles have been extensively studied (Cipriani 2007). A crucial discovery was the importance of the presence of hydroxyl groups in the crystal structure by Schaller (1916).

Amphiboles ($AB_2C_5T_8O_{22}W_2$, $C_5 = M(1)_2$, $M(2)_2$, $M(3)$) occur in many igneous and metamorphic rocks, for example in diorite, andesite, amphibolite or greenschist. They belong to the most common rock forming minerals and occur in a wide range of temperature and pressure. The appearance of certain amphiboles is indicative of certain temperature and pressure conditions. Therefore they play an important role in the metamorphic facies concept and can be used as geothermometers and geobarometers (Schumacher 2007). For this purpose it is essential to understand precisely the thermodynamic behavior of different amphiboles.

Some amphiboles may occur as asbestos, i.e. in the form of fibers with a length to diameter ratio $\geq$ 3:1 (Shukla et al. 2003). Due to their thermal stability asbestos fibers have been added as insulators to many commercially used materials, before it became clear that the exposure to amphibole asbestos can cause severe lung diseases (Klein and Philpotts 2012). This harmfulness is associated with the generation of free radicals and other reactive oxygen species like the hydroxyl radical, which is related to the availability and oxidation of iron (Kamp et al. 1992). Therefore understanding the oxidation mechanism in iron-bearing amphiboles could be useful in medical science. Furthermore it could have an application in geophysics, since the oxidation of iron in amphiboles may be the cause for the high electric conductivity that is observed in some regions of the continental crust (Wang et al. 2012). The accompanying dehydration reaction is thought to be related to intermediate-depth seismicity in subduction zones (Hacker et al. 2003).

Addison and Sharp (1962) have revealed that the ease with which divalent iron is oxidized depends on the availability of OH-groups on the crystal surface and on the Mg^{2+} and Fe^{2+} content in the mineral. The higher the Fe^{2+} content, the easier iron will be oxidized. Della Ventura et al. (2018) have achieved further interesting results by conducting a study on the dynamics of iron oxidation in riebeckite, an iron-rich amphibole, using infrared and Raman spectroscopy and combining the data with results obtained from Mössbauer spectroscopy and single-crystal structure refinement. They conclude that the oxidation proceeds in different steps: During heat treatment the O-H bonds enlarge. At a certain temperature the outermost electrons of $^{M(1)}Fe^{2+}$ and hydrogen cations from $^{W}(OH)^{-}$ start to delocalize but stay inside the crystal. The delocalization is reversible by cooling down to room temperature. Only when the kinetic energy increases at higher temperatures, H^{+}-ions and electrons are irreversible ejected from the crystal and also iron is oxidized irreversibly. Furthermore the results show that atmospheric oxygen is

needed for the reaction and that oxidation starts at the surface and then proceeds towards the interior of the crystal.

In this thesis another iron-bearing amphibole, actinolite (general chemical formula $^{A}{\square}^{B}Ca_2{}^{C}(Mg_{5-x}Fe^{2+}{}_x)Si_8O_{22}{}^{W}(OH)_2$, $x \epsilon [0.5\text{-}2.5]$), will be studied. The goal is to examine the thermal stability in nitrogen atmosphere and air and to get a picture of possible oxidation processes. There are few studies on actinolite yet, since it barely has been mined and industrially used (Shukla et al. 2003).

Raman spectroscopy is an appropriate method for studying the thermal stability and oxidation processes in amphiboles because of several reasons. With Raman spectroscopy it is possible to detect light elements like hydrogen, which is essential for examining hydrous minerals. Moreover it is perfect for detecting a process that takes place at the crystal surface, since the penetration depth of the laser is only approximately 1 µm. Besides, it is fast, non-destructive, easy to handle and no sample preparation is needed. An additional motivation for using Raman spectroscopy is to possibly find out more about how the presence of divalent and trivalent iron, respectively, influence the Raman spectra. Until now only with Mössbauer spectroscopy it is possible to distinguish between the two oxidation states and it would be useful to find another method that can be used for this as well.

1.1 The structure and chemistry of amphiboles

Amphiboles are hydrous double chain silicates represented by the general chemical formula $AB_2C_5T_8O_{22}W_2$. The characteristic double chains build 6-membered TO_4-rings (Figure 1). The different positions can be occupied by various ions. The A-site can be vacant (□), partly filled or filled by Na^+, K^+, Ca^{2+}, Pb^{2+} or Li^+; the B-site can be occupied by Na^+, Ca^{2+}, Mn^{2+}, Fe^{2+}, Mg^{2+} or Li^+; the octahedrally coordinated C-site by Mg^{2+}, Fe^{2+}, Mn^{2+}, Al^{3+}, Fe^{3+}, Mn^{3+}, Cr^{3+}, Ti^{4+} or Li^+; the tetrahedrally coordinated T-site by Si^{4+}, Al^{3+}, Ti^{4+} or Be^{2+} and the W-site can be occupied by OH^-, O^{2-}, F^- or Cl^- (Hawthorne et al. 2012). In crystallography the B-site is labeled with M(4). The C-site consists of three crystallographically distinguishable sites, which are labeled with M(1), M(2) and M(3). There are two M(1), two M(2) sites and one M(3) site. At the T-site may be distinguished between T(1) and T(2). Furthermore it is differentiated between bridging oxygen atoms that are shared between two T-site tetrahedra (O(5), O(6), O(7)) and non-bridging oxygen atoms (O(1), O(2), O(3), O(4)) (Hawthorne and Oberti 2007). Most amphiboles crystallize in the monoclinic system but there are also orthorhombic ones.

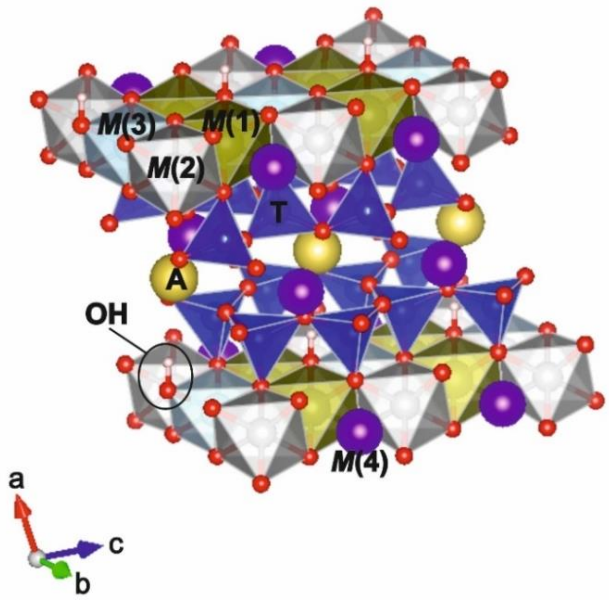

Figure 1: The structure of a monoclinic amphibole with space group *C*2/*m* (yellow: A-site cations, violet: M(4)-site cations, dark blue: T-site tetrahedra, olive green: M(1) site octahedra, grey: M(2) site octahedra, light blue: M(3) site octahedra, red: oxygen anions, white: hydrogen cations). This figure was prepared using the VESTA software package (Momma and Izumi 2008) with the structural data by Welch and Knight 1999). (Color online)

1.1.1 Amphiboles on the tremolite ferro-actinolite join

Amphiboles on the tremolite - ferro-actinolite join, $\square Ca_2Mg_5Si_8O_{22}(OH)_2$ – $\square Ca_2Fe^{2+}{}_5Si_8O_{22}(OH)_2$, are assigned to the subgroup of the calcium amphiboles. They crystallize in the monoclinic system. Tremolite may have a composition ranging from $\square Ca_2Mg_5Si_8O_{22}(OH)_2$ to $\square Ca_2Mg_{4.5}Fe^{2+}{}_{0.5}Si_8O_{22}(OH)_2$ and is found in low-grade metamorphic rocks of contact and regional metamorphism. Typically, it forms in metamorphosed Mg-rich carbonates by reaction between dolomite and quartz. The intermediates in the series from $\square Ca_2Mg_{<4.5}Fe^{2+}{}_{>0.5}Si_8O_{22}(OH)_2$ to $\square Ca_2Mg_{2.5}Fe^{2+}{}_{2.5}Si_8O_{22}(OH)_2$ are named actinolite. Actinolite is a characteristic mineral for metabasites in the greenschist facies. It also occurs in thermally metamorphosed impure dolomites, in the amphibolite and epidot-amphibolite facies and in some glaucophane schists. Amphiboles with a composition ranging from

$\square Ca_2Mg_{<2.5}Fe^{2+}{}_{>2.5}Si_8O_{22}(OH)_2$ to $\square Ca_2Fe^{2+}{}_5Si_8O_{22}(OH)_2$ are called ferro-actinolite. They mainly occur in metamorphosed iron formations. (Hawthorne et al. 2012; Deer et al. 2013)

1.2 The oxidation process in Fe-bearing amphiboles

The oxidation and dehydroxylation reaction in Fe-bearing hydrous minerals can be formulated as (Addison and Sharp 1962):

$$4\ Fe^{2+} + 4\ OH^- + O_2 \rightarrow 4\ Fe^{3+} + 4\ O^{2-} + 2\ H_2O \qquad (1)$$

Thus, the oxidation of one Fe^{2+} cation requires the reduction of one OH^- group by ejection of H^+ from the crystal. Two ejected hydrogen cations combine with external (atmospheric) oxygen and form one water molecule. The reaction (1) is accompanied by the release of 4 electrons (Della Ventura et al. 2018).

Fe^{3+} cations are smaller than Fe^{2+} cations (Addison and Sharp 1962) and have a higher electronegativity (Li and Xue 2006). Therefore it is expected that oxidation causes a slight change in the crystal geometry and affects the interaction between the atoms.

Mössbauer data from Ishida et al. (2002) have shown that in some amphiboles of the tremolite – ferro-actinolite series Fe^{2+} located at the M(1) and M(3) sites is oxidized faster than Fe^{2+} located at the M(2) site, while results presented by Oberti et al. (2018) reveal that in riebeckite only $^{M(1)}Fe^{2+}$ is affected.

2 Materials and methods

2.1 Studied sample

For the high-temperature experiments in this study an actinolite sample with the crystal-chemical formula $^{A}(Na_{0.16}K_{0.01})^{B}(Ca_{1.74}Fe^{2+}{}_{0.24}Mn^{2+}{}_{0.02})^{C}(Mg_{4.33}Fe^{2+}{}_{0.53}Al_{0.1}Cr^{3+}{}_{0.05})^{T}(Al_{0.18}Si_{7.82})O22$ $W(OH_{1.99}F_{0.01})$ was used. The sample was kindly provided by the Mineralogical Museum of the University of Hamburg and the chemistry was examined by electron microprobe analyses (EMPA) as part of a master thesis by Leissner (2014). The actinolite sample originates from the Zillertal, in Austria from a low-grade regional metamorphic affected region. The color is dark green (Figure 2).

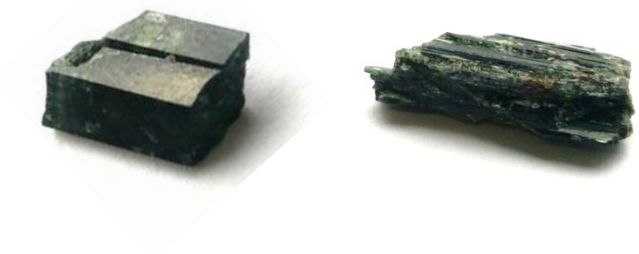

Figure 2: Actinolite sample examined in this study (size of the crystals: >10 mm)

2.2 Raman spectroscopy

Spectroscopic methods are used to examine the interaction between electromagnetic radiation or a particle beam and matter, which leads to a change in the energy of the system. Raman spectroscopy is a vibrational spectroscopic method based on the Raman effect, which is inelastic light scattering by atomic vibrations. The collective atomic vibrations in a crystal are called phonons. There are two different types of phonons: acoustic phonons, which oscillate in- phase and optical phonons that oscillate out-of-phase. In Raman spectroscopy only the radiation scattered by optical phonons is detected. The radiation used to irradiate a sample during an experiment is in the visible, ultraviolet or near-infrared spectrum and originates from a monochromatic laser beam with the electric field strength E and angular frequency ω_0. The electric field strength E at a given time t is described by the equation:

$$E = E_0 \cos 2\pi\omega_0 t,$$

where E_0 is the vibrational amplitude of the laser. Due to the irradiation of the sample an electric dipole moment P is induced:

$$P = \alpha E$$

where α is the polarizability, which is a proportionality constant that describes how easy a molecule may be distorted. Since P and E are vectors with three components in the x, y and z directions, α is a second-rank tensor:

$$\alpha = \begin{bmatrix} \alpha_{xx} & \alpha_{xy} & \alpha_{xz} \\ \alpha_{yx} & \alpha_{yy} & \alpha_{yz} \\ \alpha_{zx} & \alpha_{zy} & \alpha_{zz} \end{bmatrix}$$

where $\alpha_{xy} = \alpha_{yx,}$ $\alpha_{xz} = \alpha_{zx}$ and $\alpha_{yz} = \alpha_{zy,}$ since the Raman polarizability tensor is symmetric. A vibrational mode is Raman-active if a change in polarizability occurs during the dynamic atomic displacements, thus, one of the components must not be zero.

From quantum mechanical point of view, during the electric dipole moment is induced, the phonons in the crystal get excited to a virtual energy state and then drop back. The incident radiation is scattered either elastically or inelastically (Figure 3). When a phonon is at the vibrational ground state and after getting excited drops back to the ground state, the light is scattered elastically, which means that the scattered radiation has the same frequency as the incident radiation (ω_0). This is called Rayleigh scattering. The inelastic scattering of light is called Raman scattering, which comprises two processes. The first is the Stokes scattering, which arises from phonons that do not drop to the ground state after the excitation but to a higher energy level absorbing energy from the incident radiation ($\omega_0 - \omega_{m,}$ where ω_m is a vibrational angular frequency, in crystals also called phonon wavenumber). The second is the anti-Stokes scattering that arises from phonons that initially are at an excited internal energy level and after getting excited drop down to the ground state. In this case, the incident radiation gains energy ($\omega_0 + \omega_m$).

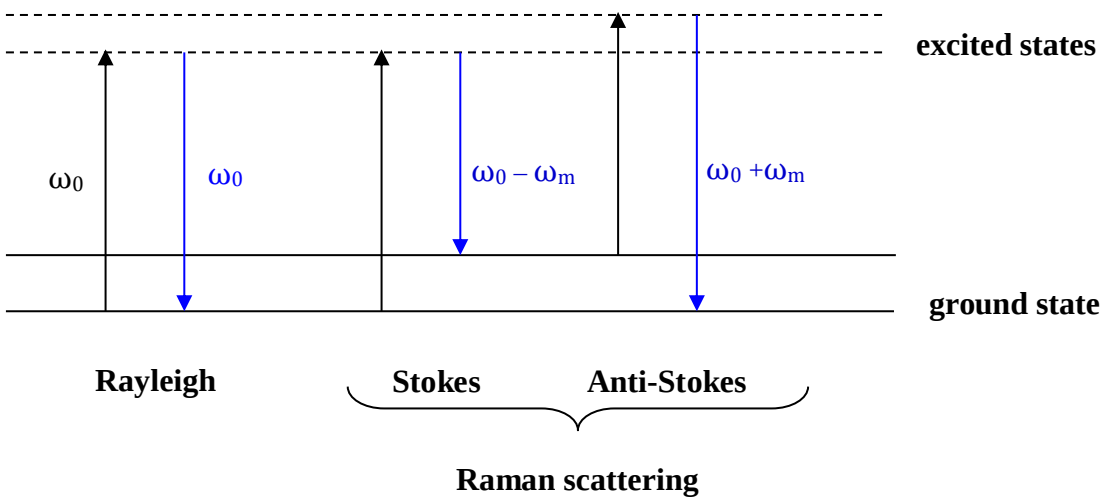

Figure 3: Rayleigh and Raman scattering processes

In Raman spectroscopy, the difference between the frequency of the incident and the scattered light, thus, the vibrational frequency ω_m, is measured as a shift, the so-called Raman shift. The peaks arising from the Stokes process are shifted to lower wavenumbers and anti-Stokes peaks are shifted to higher wavenumbers with respect to the incident frequency. The intensity of the Rayleigh scattered light is the strongest (10^{-4} times the intensity of the incident light) because most phonons are scattered elastically. The intensity of the Stoke scattered light is about 10^{-7} times the intensity of the incident radiation and the intensity of the anti-Stokes scattered light is even weaker. This is because at room temperature the majority of phonons are at the ground state. Hence, the Stokes process is more likely to happen than the anti-Stokes process. Since both provide the same information, usually only the Stokes side of the spectrum is measured.
The measured peaks provide information about the chemistry and structural properties of the sample, since the peak position ω depends on the masses of the vibrating atoms and on the strength of the chemical bonds via the correlation

$$\omega = \sqrt{\frac{K}{\mu}}$$

where K is the force constant of the chemical bond and $\mu = \frac{m1m2}{m1 + m2}$ is the reduced mass of the vibrating atoms. The bonds are regarded as springs (Figure 4) and the vibrations as harmonic oscillations. (Ferraro et al. 2003; Kakkar 2015; Nasdala et al. 2004)

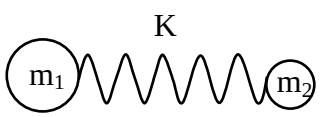

Figure 4: Sketch of a chemical bond with the force constant K between two atoms with the masses m_1 and m_2

2.2.1 Raman spectroscopy of amphiboles

Before performing vibrational spectroscopic experiments, it is helpful to perform a group theory analysis and to consider in which spectral ranges the different vibrational modes will occur.

2.2.1.1 Group theory

The application of group theory allows predicting which vibrational modes will be observed in a spectroscopic measurement. A vibrational mode can be Raman active, infrared active or silent. If the vibrational mode causes a change in the bond polarizability and the induced dipole moment is attributed to the difference between the positively charged nucleus and the center of gravity of the surrounding, negatively charged electron shell, it is allowed to be Raman active. If a change in the dipole moment is due to the mismatch between the center of gravity of positively charged ions and the center of gravity of negatively charged ions, the vibrational mode is allowed to be infrared active. The Bilbao Crystallographic server (www.cryst.ehu.es) can be used to calculate how many Raman and infrared active modes are expected. The only information needed is the space group of the crystal and the occupied Wyckoff positions.
In group theory there is a character table for each point group that provides a lot of information. The character table for the point group 2/*m* is shown in Table 1.

Table 1: Character table for the point group 2/*m* (after Kroumova et al. 2003)

C_{2h} (2/*m*)	1	2	-1	m	functions
A_g	1	1	1	1	x^2, y^2, z^2, xy, J_z
B_g	1	-1	1	-1	xz, yz, J_x, J_y
A_u	1	1	-1	-1	z
B_u	1	-1	-1	1	x, y

In the first column, all symmetry species that occur in the respective point group are listed represented by Mulliken symbols. In monoclinic crystals of the point group 2/*m* only symmetry species occur that are symmetric (A) or anti-symmetric (B) with respect to the principal axis of symmetry; and symmetric (A_g, B_g) or anti-symmetric (A_u, B_u) with respect to a center of symmetry. A and B modes are one dimensional representations. A_g and B_g modes are Raman active, while A_u and B_u modes are infrared active. All symmetry operations occurring in the point group 2/*m* are displayed in the orange fields in the first row (Table 1): an one-fold rotation axis, a two-fold rotation axis, a center of symmetry and a mirror plane perpendicular to the two-fold rotation axis. In the last column ("functions") of Table 1 the selection rules are listed. Considering the polarizability tensors (Table 2), it can be seen which are the selection rules for the Raman active modes (Tuschel 2014).

Table 2: Polarizability tensors of the Raman active modes (after Kroumova et al. 2003)

A_g			B_g		
xx	.	xz	.	xy	.
.	yy	.	yx		yz
zx	.	zz	.	zy	.

xx <=> x^2, yy <=> y^2, zz <=> z^2

The occupation of the Wyckoff positions and the corresponding Raman active modes in amphiboles with space group *C*2/*m* are shown in Table 3. The Wyckoff position is composed of a number, which indicates the multiplicity (the number of equivalent atoms in the unit cell generated by symmetry) and a letter that has no physical meaning.

Table 3: Crystallographic sites, occupied Wyckoff positions (after Evans and Yang 1998) and Raman active modes in amphiboles with space group *C*2/*m* (after Kroumova et al. 2003)

Crystallographic site	**Wyckoff position**	**Fractional coordinates**	**Raman active modes**	
			A_g	**B_g**
T1	8j	x, y, z	3	3
T2	8j	x, y, z	3	3
O1	8j	x, y, z	3	3
O2	8j	x, y, z	3	3
O3	4i	x, y, 0	2	1
O4	8j	x, y, z	3	3
O5	8j	x, y, z	3	3
O6	8j	x, y, z	3	3
O7	4i	x, y, 0	2	1
M1	4h	½, 0, z	1	2
M2	4g	0, 0, z	1	2
M3	2a	0, 0, 0	.	.
M4	4h	½, 0, z	1	2
A	2b	0, 0, ½	.	.
H1	4i	x, y, 0	2	1
			$\sum_{Ag}$ 30	$\sum_{Bg}$ 30

In total, there are 60 Raman active modes. Which of them will be observed in a spectrum is determined by the orientation in that the crystal is measured with respect to the polarization of the laser. The different configurations can be expressed by Porto's notation: A(BC)D, where A

and D represent the propagation direction of the incident ($\vec{k}_0$) and the scattered ($\vec{k}_s$) light, respectively, and B and C represent the polarization direction of the incident ($\vec{E}_0$) and the scattered light ($\vec{E}_s$), respectively. The possible configurations and Raman active modes for measurements in backscattering geometry are shown in Figure 5 and Table 4.

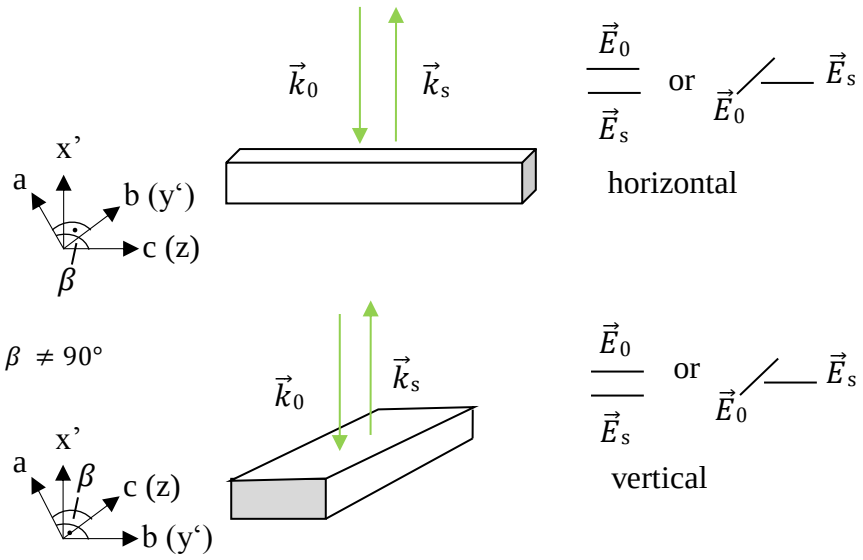

Figure 5: Sketch of the possible orientations of the sample measured in backscattering geometry; due to the variation in the cleavage planes, $\bar{a}$ and $\bar{b}$ can be rotated within the (x', y') plane.

Table 4: Possible configurations and the respective Raman active modes

Orientation of the sample	**Polarization of the laser**	**Porto's notation**	**Detected polarizability tensor components**	**Raman active modes**
Horizontal	HH	$\bar{x}$'(zz)x'	zz, xx	A_g
Horizontal	VH	$\bar{x}$'(y'z)x'	yz, yx, xz	A_g, B_g
Vertical	HH	$\bar{x}$'(y'y')x'	yy, xx	A_g
Vertical	VH	$\bar{x}$'(zy')x'	zx, zy, xy	A_g, B_g

HH = parallel polarized, VH = cross polarized

2.2.1.2 Peak assignment

Due to the complex structure of amphiboles it is difficult to assign all of the observed peaks in the spectra to the corresponding vibrational modes. Especially the origin of the spectral bands below 625 cm^{-1} is not completely understood yet. Different opinions are found in literature. In this study, the following assignments have been taken into account (Figure 6): The range below ~425 cm^{-1} is supposed to be dominated by vibrations of the MO_6 octahedra and in addition may be influenced by TO_4-external modes and OH libration and translation. Raman bands between ~450 cm^{-1} and 625 cm^{-1} are thought to be generated by bending of the Si-O-Si and O-Si-O bonds. The spectral range from ~650-750 cm^{-1}, where in Raman spectra of amphiboles typically appears the most intense peak, is commonly ascribed to the so-called SiO_4-ring breathing mode, which is also known as Si-O-Si bending mode. The peaks in the range from ~950-1130 cm^{-1} are assigned to SiO_4-tetrahedra stretching vibrations. The Si-O vibrations involving oxygen atoms that are shared between two SiO_4-tetrahedra (Si-O_b-Si, O_b=bridging O) are expected to appear in the spectral range from 1000-1130 cm^{-1} and the Si-O vibrations involving non-bridging oxygen atoms (O-Si-O) in the range from ~950-1000 cm^{-1}. O-H bond stretching vibrations are detected in the spectral range from ~3500-3700 cm^{-1}. (Apopei and Buzgar 2010; Susta et al. 2018; Leissner et al. 2015)

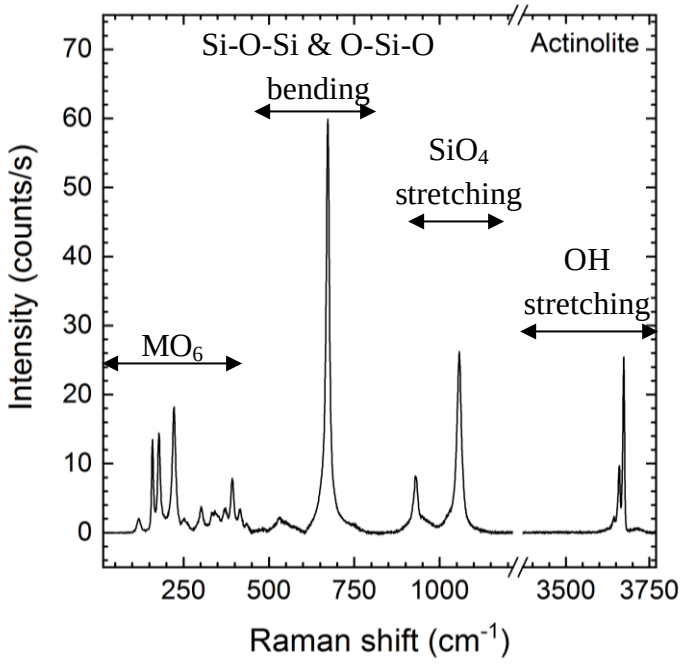

Figure 6: The vibrational modes in amphiboles

2.3 Experimental conditions

The Raman scattering experiments were performed using a Horiba Jobin-Yvon T64000 triple-grating monochromator spectrometer equipped with an Olympus BX41 microscope and a LN_2-cooled Symphony CCD detector. The 514.532 nm green line of a Coherent Innova 90C FreD Ar^+ Laser was used to irradiate the sample. The laser beam was focused through a 50x LWD microscope objective on a spot with a diameter of ~2 µm on the surface of the crystal. The output laser power was 0.6 W. For reducing the laser power filter 1 (0.1 transmittance) was used, thus, the laser power on the surface was 6.55 mW. The Raman spectra were measured in backscattering geometry in the spectral ranges 15-1215 cm^{-1} and 3370-3770 cm^{-1}. The spectral resolution was ~2.0 cm^{-1}. At room temperature Raman spectra were collected focusing the laser on different points of the crystal surface to prove homogeneity of the sample and repeatability of the spectra. All measurements at different temperatures were performed with vertical orientation of the sample and parallel polarized light, thus with scattering geometry $\bar{x}$'(y'y')x'.

In situ high-temperature Raman experiments were done in nitrogen atmosphere and in ambient atmosphere. For generating a nitrogen atmosphere around the sample, a LINKAM THMS-E600 heating/cooling stage was used, which provides a temperature accuracy of ±0.1 K. The cell was heated to 313 K to set N_2 purge. There was strong luminescence that disappeared after a couple of minutes. After heating to 350 K there was strong luminescence again. The problem could be solved by slightly changing the spot. Raman spectra were collected every 20 K cooling down the sample to 100 K. While reheating to room temperature another spectrum was collected at 210 K. Next the sample was heated to 870 K collecting spectra every 50 K. After cooling down to room temperature a final spectrum was recorded.

The measurements in ambient atmosphere were performed in a LINKAM TS1200 EV-1015 heating stage with temperature accuracy ±1 K. On heating up to 1300 K Raman spectra were collected every 50 K. Another two spectra were recorded after cooling down, one 5 minutes and the other one 30 minutes after reaching the room temperature. It should be mentioned that above 1000 K the background was strongly increased due to blackbody emission.

For each measurement the heating/cooling rate was set to 10 K/min, the acquisition to 20 s and the spectrum was averaged over 10 loops. Each data collection started after 5 minutes spent at the respective temperature. In nitrogen at 870 K additional spectra were collected after 35, 80,120 and 165 minutes. In ambient atmosphere at 1300 K another spectrum was recorded after 30 minutes.

The program used for data collection was LabSpec Spectroscopy Suite Software.

2.4 Data evaluation

The data was imported in OriginPro. The Rama spectra were baseline corrected by removing the instrumental background and the background caused by photoluminescence (Figure 7). Then the Raman intensity was normalized by the Bose-Einstein population factor for Stokes processes to remove the temperature dependence:

$$I = \frac{I_0}{n(\omega, T) + 1}$$

where

$$n(\omega, T) = \frac{1}{e^{\frac{\hbar\omega}{k_B T}} - 1}$$

where ω represents the phonon wavenumber, T the Temperature, $\hbar$ the reduced Planck constant ($\hbar$ = 1.05457266x10^{-34} Js) and k_B the Boltzmann constant (k_B = 1.380658x10^{-23} J/K).

The corrected intensity was divided by the accumulation time in order to express the intensity in counts/s (Figure 7).

To determine the peak positions (ω), the full widths a half maximum (FWHMs) and the Intensities (*I*), the spectra were fitted with pseudo-Voigt functions. The pseudo-Voigt function is a weighted sum of Gaussian and Lorentzian functions:

$$y = y_0 + \mathrm{A}\left[\underbrace{\mu\frac{2}{\pi}\frac{\Gamma}{4(x-x_c)^2+\Gamma^2}}_{\text{Lorentzian function}} + \underbrace{(1-\mu)\frac{\sqrt{4ln2}}{\sqrt{\pi}\Gamma}e^{-\frac{4ln2}{\Gamma^2}(x-x_c)2}}_{\text{Gaussian function}}\right]$$

where y_0 is the offset, x_c the center, A the area, Γ the FWHM and μ the profile shape factor, with $\mu\,\epsilon[0,1]$. The Lorentzian function represents homogenous broadening of a peak, while the Gaussian function represents inhomogeneous broadening.

In the data analyses also the intensities normalized to the area of a whole spectrum

$$\mathrm{I}_n^{(i)} = \frac{\mathrm{I}^{(i)}}{\sum_i \mathrm{I}^{(i)}},$$

where i runs over all peaks, were considered.

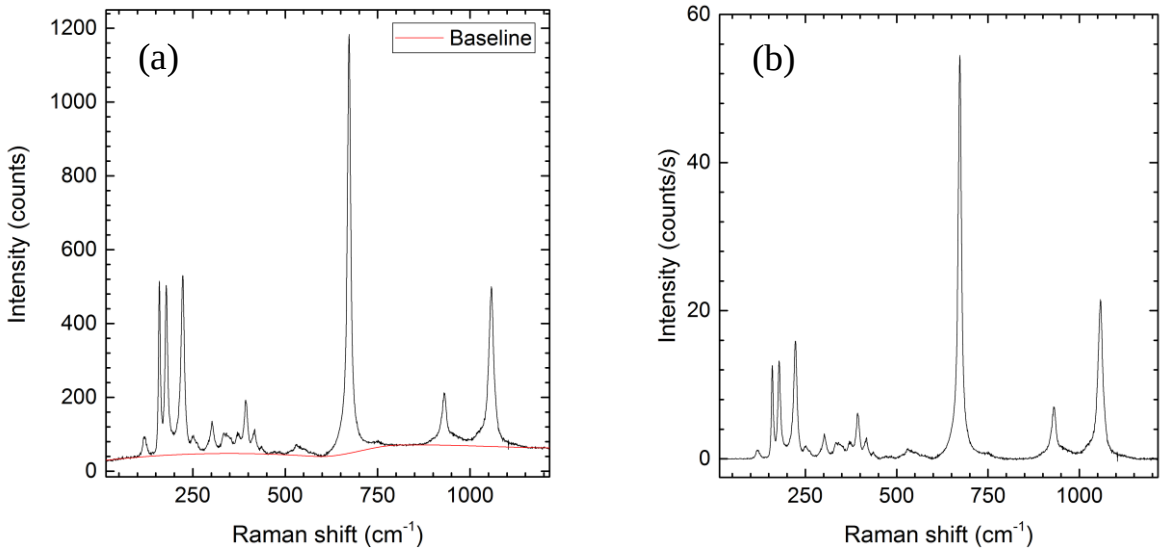

Figure 7: Baseline correction of a raw Raman spectrum (a) and the same spectrum after subtracting the baseline, removing the temperature dependence and dividing by the accumulation time (b)

3 Results and discussion

The actinolite Raman spectra recorded at different temperatures in nitrogen atmosphere and air are shown in Figure 8 and Figure 9.

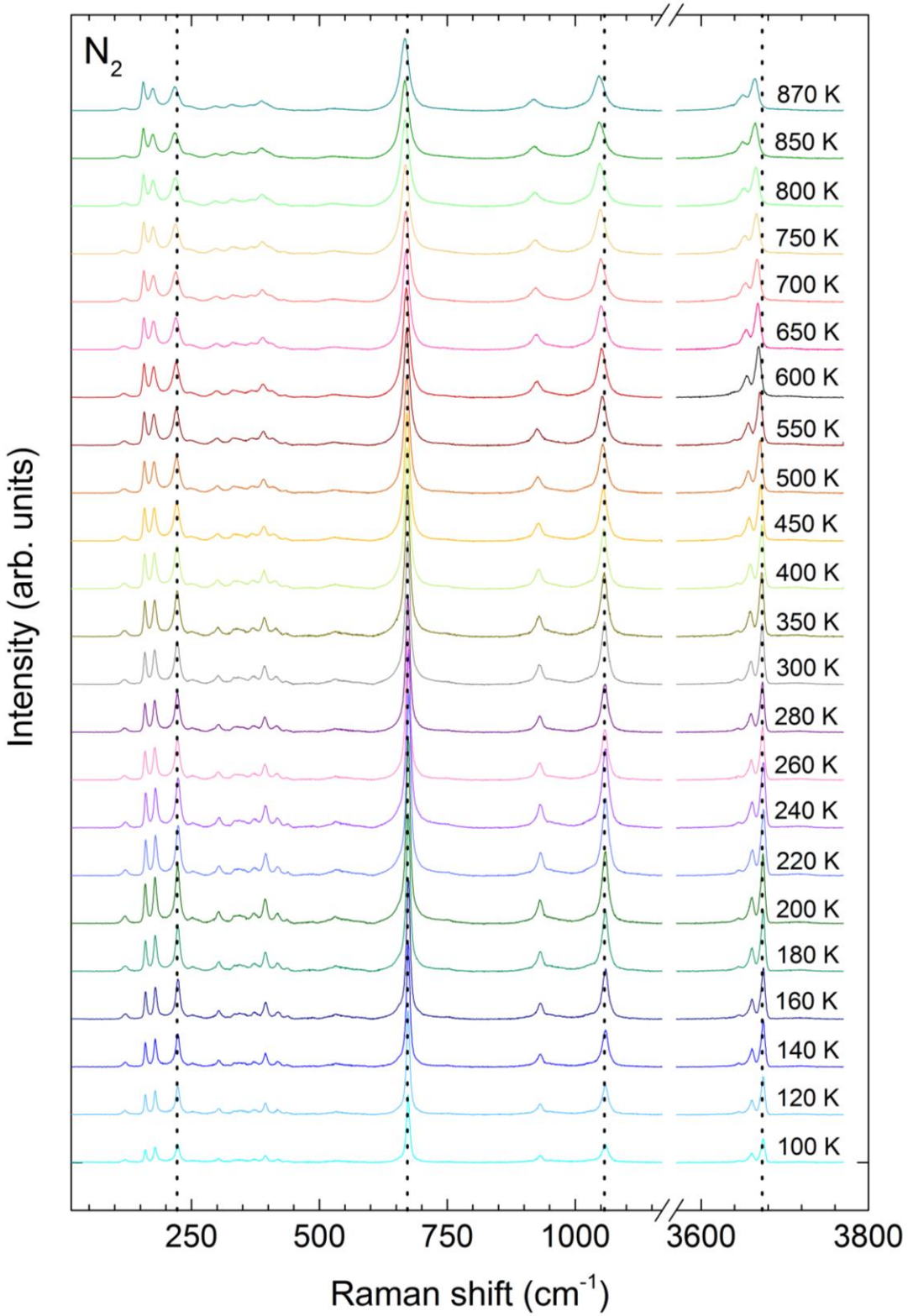

Figure 8: Baseline corrected parallel polarized Raman spectra of actinolite measured with vertical orientation of the sample at temperatures from 100-870 K in N_2. For the sake of clarity, the spectra have been offset vertically.

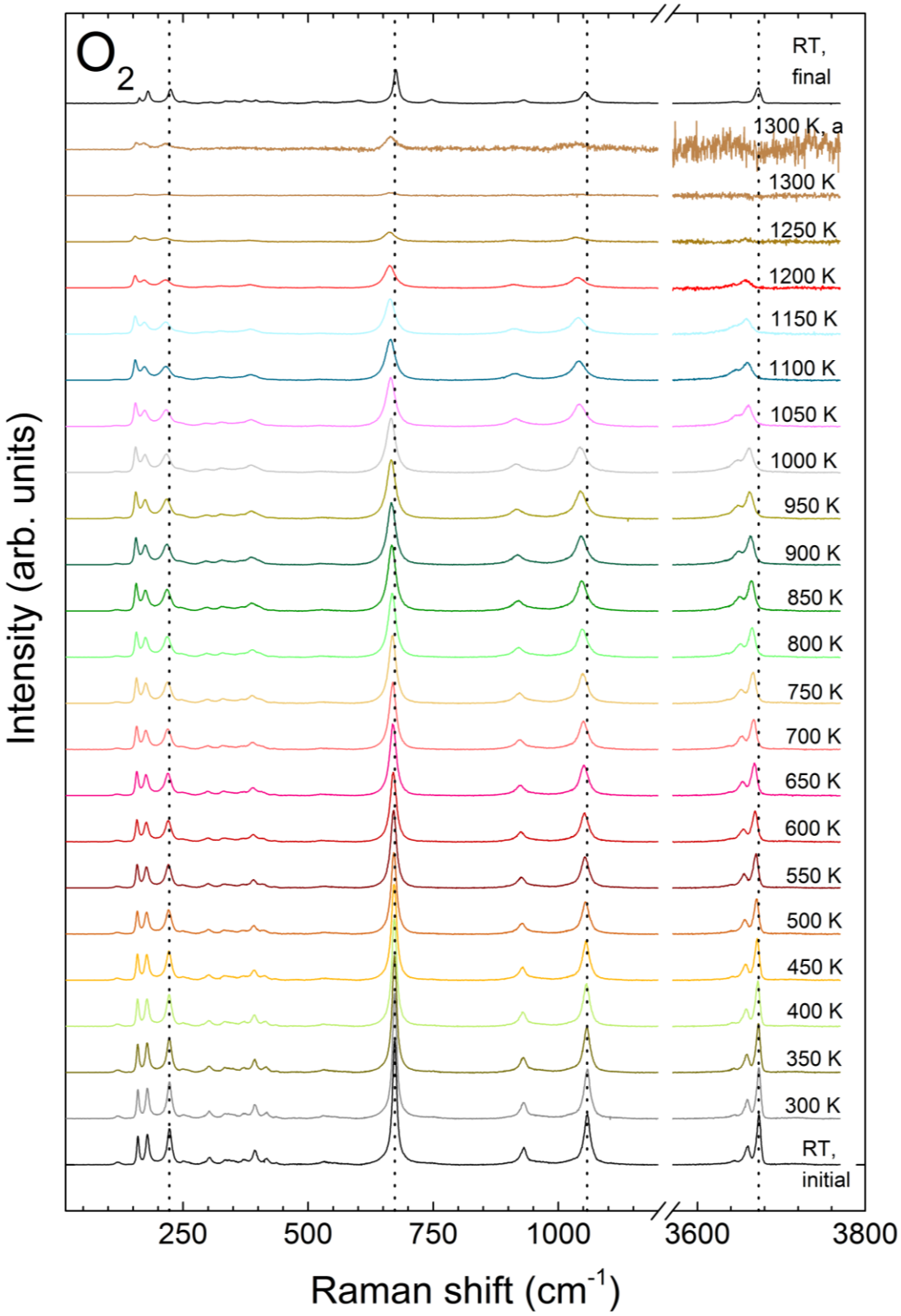

Figure 9: Baseline corrected parallel polarized Raman spectra of actinolite measured with vertical orientation of the sample at increasing temperatures up to 1300 K in O_2. For the sake of clarity, the spectra have been offset vertically.

With increasing temperature, all of the peaks show a progressive shift to lower wavenumbers and a noticeable broadening. This is the behavior usually observed for phonons in crystals with a positive thermal expansion (Della Ventura et al. 2018). The shift to lower wavenumbers can be explained as follows: when a crystal expands, the distances between the atoms increase and therefore the force constants K of the chemical bonds decrease. Since $\omega = \sqrt{K/\mu}$, the peak positions shift to lower wavenumbers. The broadening of the peaks is due to dynamical disorder in the system caused by the increasing thermal fluctuations, which in turn increases the phonon-phonon interactions and leads to a decrease in the propagation length of the individual phonons. Apart from these gradual changes, the spectra at low and high temperatures in nitrogen barely deviate from the spectrum recorded at room temperature. In air in contrast above 1000 K the overall intensity (*I*total) significantly decreases (Figure 10) and after 1250 K in range from 3370-3770 cm^{-1} no peaks are observed anymore (Figure 9). After cooling down to room temperature, they partially recover. A similar behavior has been documented for riebeckite by Della Ventura et al. (2018). The partial recovery of the OH-stretching peaks suggests that the amount of OH-groups is reduced. This can be confirmed by considering the total intensity of the OH-stretching vibrations ($I\text{total}_{\text{OH-stretching}}$) in relation to the total intensity of the framework vibrations ($I\text{total}_{\text{framework}}$) (Figure 11). At the final room temperature the $I\text{total}_{\text{OH-stretching}}$ ratio is slightly reduced indicating that indeed some hydrogen has been lost. During the heat treatment it drastically drops at temperatures above 1150 K indicating the delocalization of H^+ cations.

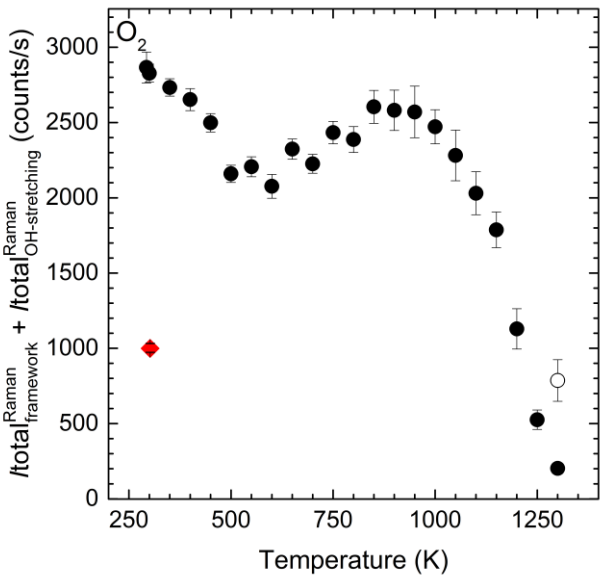

Figure 10: The total intensity of the vibrational modes in actinolite on heating in air, where ○ represents the intensity after 30 minutes spent at 1300 K and ♦ the intensity at the final RT. If not visible, the errors lie within the symbols.

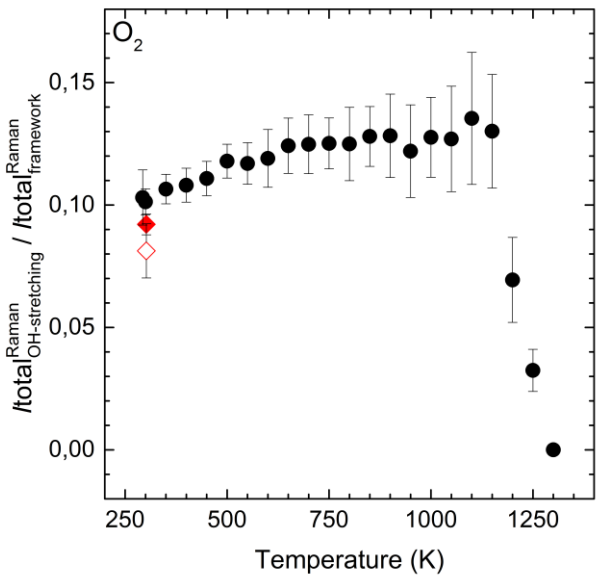

Figure 11: The total intensity of the OH-stretching vibrations divided by the total Intensity of the framework vibrations on heating in air, where ◊ is the value obtained for 5 minutes after cooling to RT and ♦ for after 30 minutes.

The final spectrum recorded at room temperature in air does not only show a change in the OH-stretching region but also in the spectral range where the framework vibrations are active. Since

it is expected that divalent iron is oxidized during the heat treatment, the changes will be examined assuming that they are caused by iron-oxidation and dehydroxylation.
It is worth mentioning, that the color of the sample after the heat treatment has changed from dark green to dark brown, which also hints at the presence of trivalent iron.
In this work the spectral bands in the range from 100-230 cm^{-1}, near 673 cm^{-1}, from 900-1100 cm^{-1} and from 3600-3770 cm^{-1}will be examined by considering the temperature trends of phonon wavenumbers (ω), widths (full widths at half maximum, FWHMs) and fractional intensities (I_n), in the following also referred to as normalized intensities.

3.1 Raman scattering of the framework vibrations:

The $\bar{x}$'(y'y')x' Raman scattering in the range from 15-1215 cm^{-1} was fitted with 22 peaks (Figure 12). Several peaks generated by different phonon modes, which all should arise from A_g modes, were selected as representatives for the corresponding cation-oxygen cluster. Peak 1 (~120 cm^{-1}), peak 2 (~160 cm^{-1}), peak 3 (~179 cm^{-1}) and peak 4 (~222 cm^{-1}) result from MO_6 vibrations and therefore are directly sensitive to the M-site occupancy. Furthermore, the SiO_4-breathing mode (peak 17, ~673 cm^{-1}) will be analyzed and in the SiO_4-stretching mode peak 19 (~930 cm^{-1}) and peak 22 (~1057 cm^{-1}) will be considered.

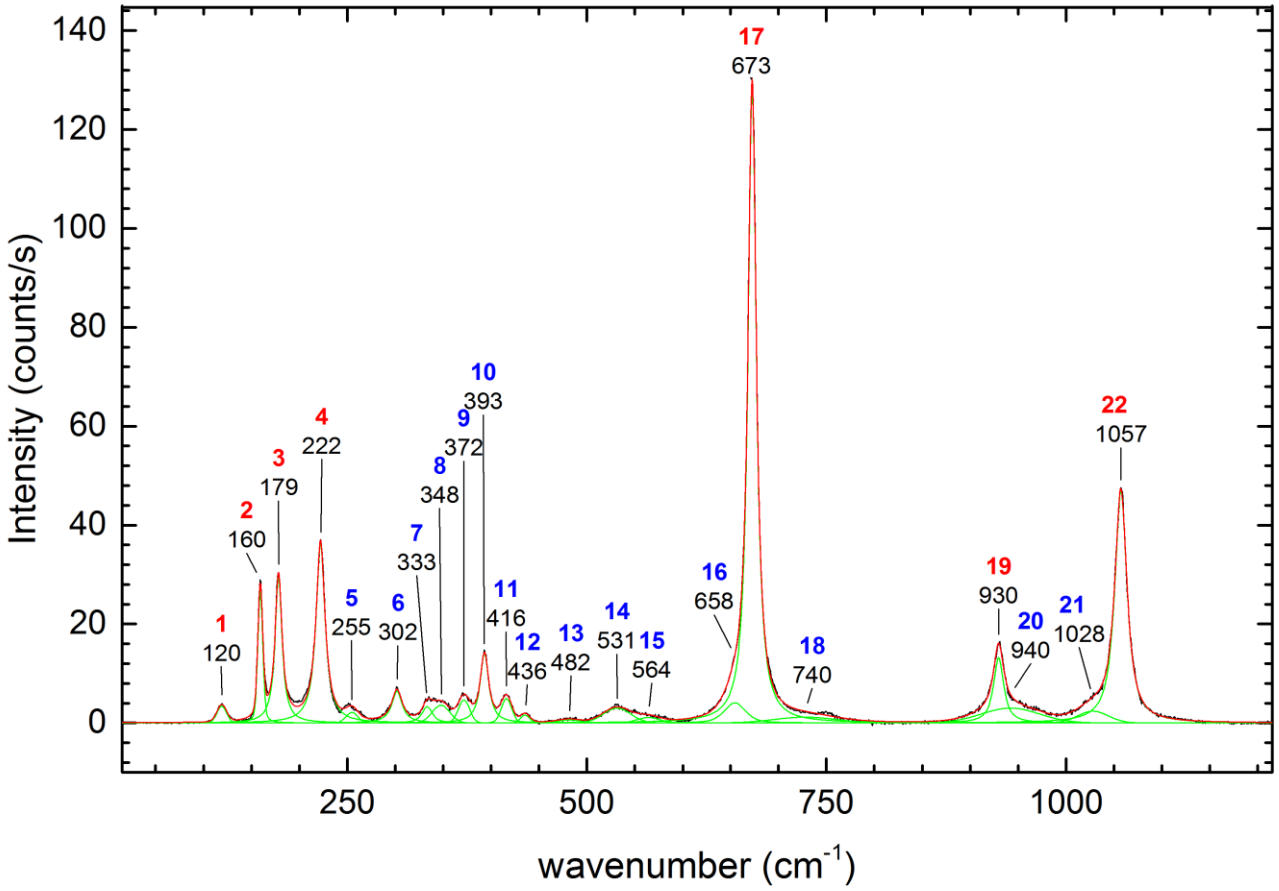

Figure 12: Peak fitting of the framework vibrations and labelling of the peaks. The black numbers designate the peak positions at room temperature in cm^{-1}. Peaks that will be analyzed are labelled in red.

3.1.1 The octahedral MO_6 mode

The temperature dependence of the phonon wavenumbers ω and the FWHMs Γ of peak 1 (~120 cm^{-1}), peak 2 (~160 cm^{-1}), peak 3 (~179 cm^{-1}) and peak 4 (222 cm^{-1}) can be seen in Figure 14. On cooling from room temperature to 100 K in N_2 the peak positions gradually shift to higher wavenumbers, in accordance with theory. This indicates a strengthening of the chemical bonds due to the shrinking of the unit-cell volume. However, the values at 220 K and 240 K deviate from the trend line and below 160 K ω shifts back to lower wavenumbers. Neither for the deviation at 220 K and 240 K nor for the maximum at 160 K could be found an explanation. These discontinuities are also observed in the raw spectra (Figure 13). Hence, there has not been a mistake during the peak fitting. During the experiment no abnormalities have been noted.

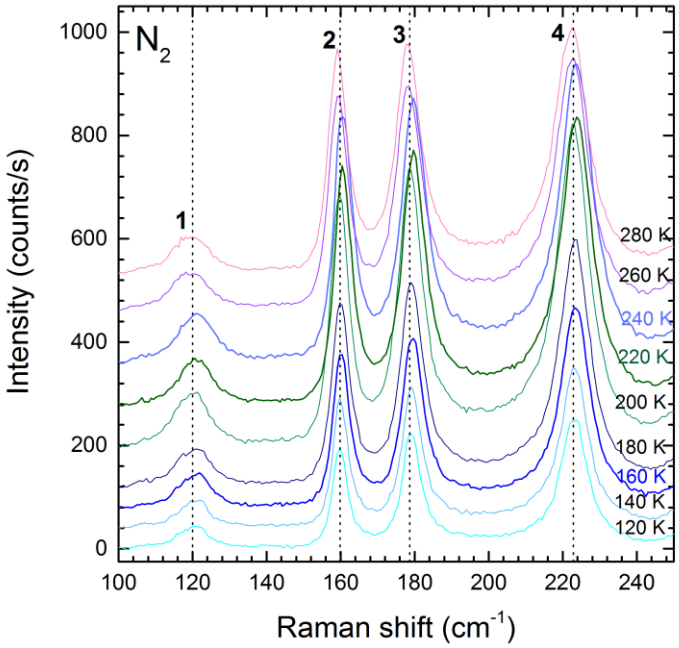

Figure 13: Raw Raman spectra in the range from 100-250 cm^{-1} at temperatures from 120-280 K.

Nevertheless, the jump at 220 K and 240 K is likely to be a result of a discontinuity in the experiment maybe caused by bad focusing. The maximum at 160 K instead could indicate that something is happening inside the crystal at low temperatures. A hint could be hat $\Gamma_{120cm^{-1}}$ exhibits a minimum at 140 K and increases significantly when cooling further down. Thus, there is a growing dynamical disorder at lower temperatures. This behavior should be examined by doing further low temperature experiments with amphiboles.

On heating, the peak positions gradually shift to lower wavenumbers. In nitrogen, they recover when cooling down to room temperature. In air, the peaks at the final room temperature appear slightly shifted to higher wavenumbers. Peak 2 shows a minimum in the peak position at 1200 K. This could be indicative of a change in the geometry of the MO_6 octahedra which occurs when smaller Fe^{3+} cations replace larger Fe^{2+} cations. The FWHMs of peak 2, 3, and 4 gradually increase with higher temperatures in nitrogen as well as in air. Peak 1 in contrast slightly gets narrower in air and slightly broadens in N_2. After cooling down to room temperature in nitrogen, all FWHMs recover. In air, peak 3 and 4 appear a little broader.

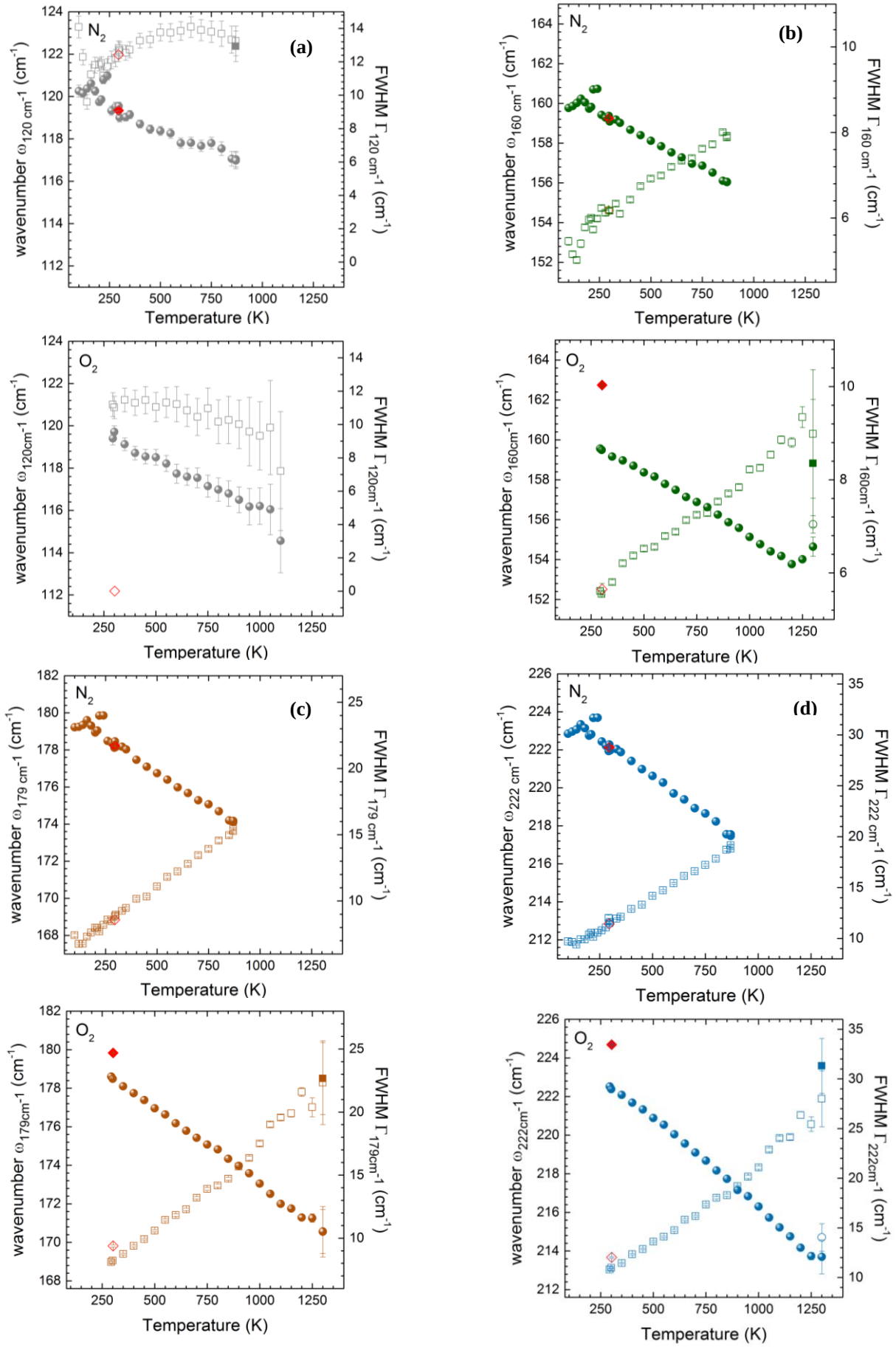

Figure 14: Temperature dependence of phonon wavenumber ω (circles, ●) and FWHM Γ (squares, □) in N_2 and air. ○ and ■ represent ω and Γ at 1300 K after 30 minutes (or at 870 K in N_2 after 60 minutes, if there is a deviation). The values obtained after the final cooling are displayed by diamonds (♦, ◊).(a): peak 1, (b): peak 2, (c): peak 3, (d): peak 4. If not visible, the error bars are within the symbols.

The evolution of the fractional intensities with temperature of the peaks 1, 2, 3 and 4 can be seen in Figure 15. $I_{n\ 120cm^{-1}}$ gradually decreases with increasing temperature, while $I_{n\ 160cm^{-1}}$, $I_{n\ 179cm^{-1}}$ and $I_{n\ 222cm^{-1}}$ slightly increase. In air peak 1 disappears above 1150 K and does not recover when cooling down to room temperature (Figure 15, Figure 16). This vanishing could be caused by temperature induced diffusion of cations, which leads to site occupancy disorder. It is also possible that peak 1 is directly related to the amount of Fe^{2+} at the C site.
Peak 2 appears with a decreased fractional intensity in the final spectrum (Figure 15, Figure 16). The normalized intensities of peak 3 and peak 4 in contrast have increased. These changes in intensity should be directly related to the amount of oxidized iron.

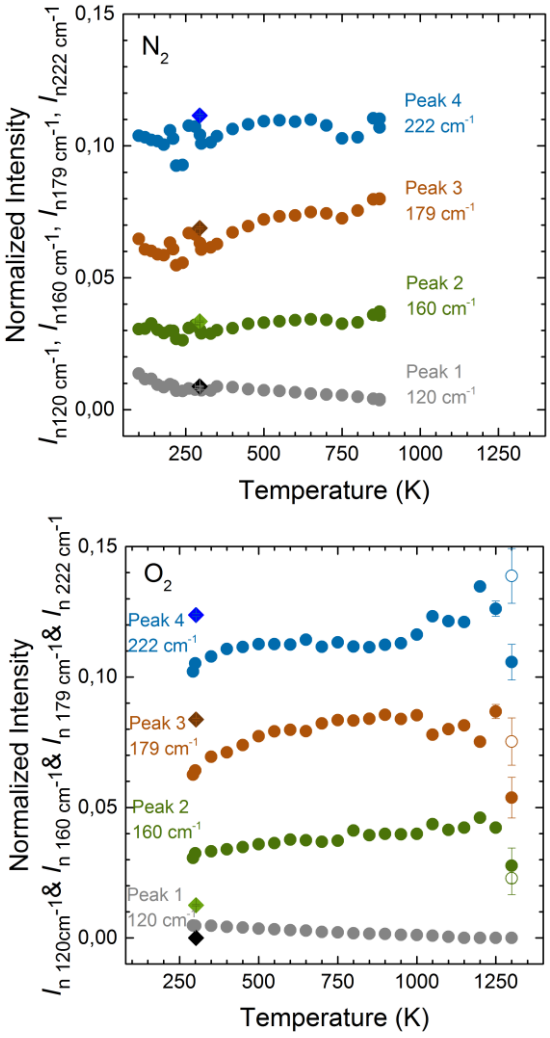

Figure 15: Temperature dependence of $I_{n\ 120cm^{-1}}$, $I_{n\ 160cm^{-1}}$, $I_{n\ 179cm^{-1}}$ and $I_{n\ 222cm^{-1}}$ in N_2 and O_2. ○ is I_n at 1300 K after 30 minutes and ♦ is I_n after cooling to room temperature. If not visible the error bars are within the symbols.

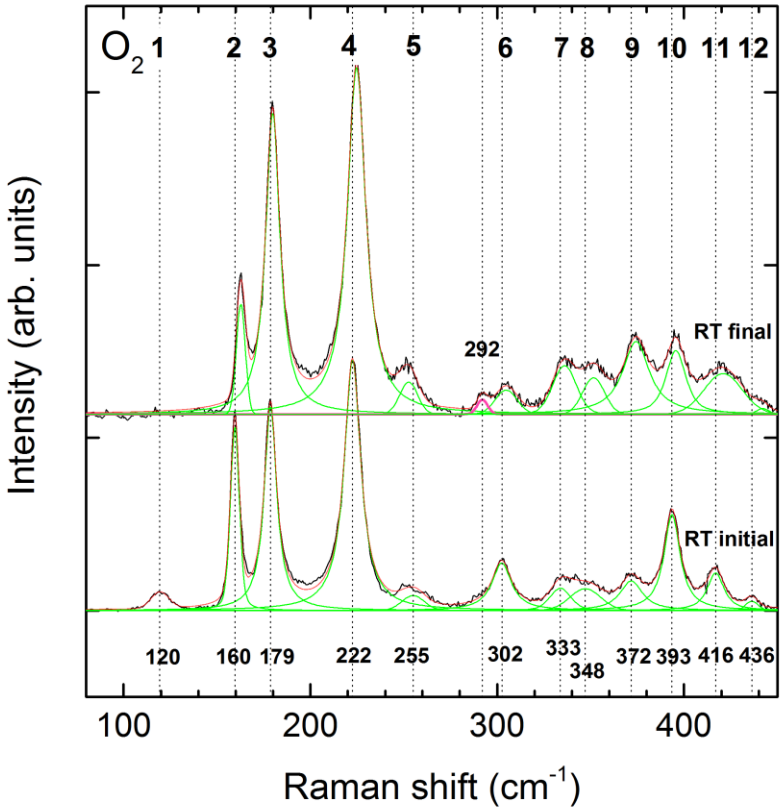

Figure 16: Initial and final Raman spectrum at room temperature in the spectral range from 100-450 cm^{-1}. For the sake of clarity, the spectra have been normalized to the strongest peak in the spectrum (peak 17) and are offset vertically.

Taking a look at the other peaks observed in the octahedral MO_6 mode in the initial and final spectrum at room temperature the following changes should be noted: A new peak is observed at ~292 cm^{-1}. It may have been present before the heat treatment but has not been fitted due to its weak intensity and peak overlapping. Furthermore, the fractional intensities of the peaks at ~302cm^{-1} (peak 6) and ~393 cm^{-1} (peak 10) have slightly decreased, while those of the peaks at ~372 cm^{-1} (peak 9) and at ~416 cm^{-1} (peak 11) have increased.

3.1.2 The SiO_4-ring breathing mode

The temperature trends of the phonon wavenumber ω and the FWHM Γ of peak 17 (~673 cm^{-1}), the most intense peak in the whole spectrum, are displayed in Figure 17. At low temperatures, ω shows the same behavior as the peaks in the MO_6 mode: a shift to higher wavenumbers with a maximum at 160 K and also the values at 220 K and 240 K deviate from the trend line.

On heating, the peak position gradually shifts to higher wavenumbers while the FWHM increases. In nitrogen, this evolution is linear and reversible by cooling down to room

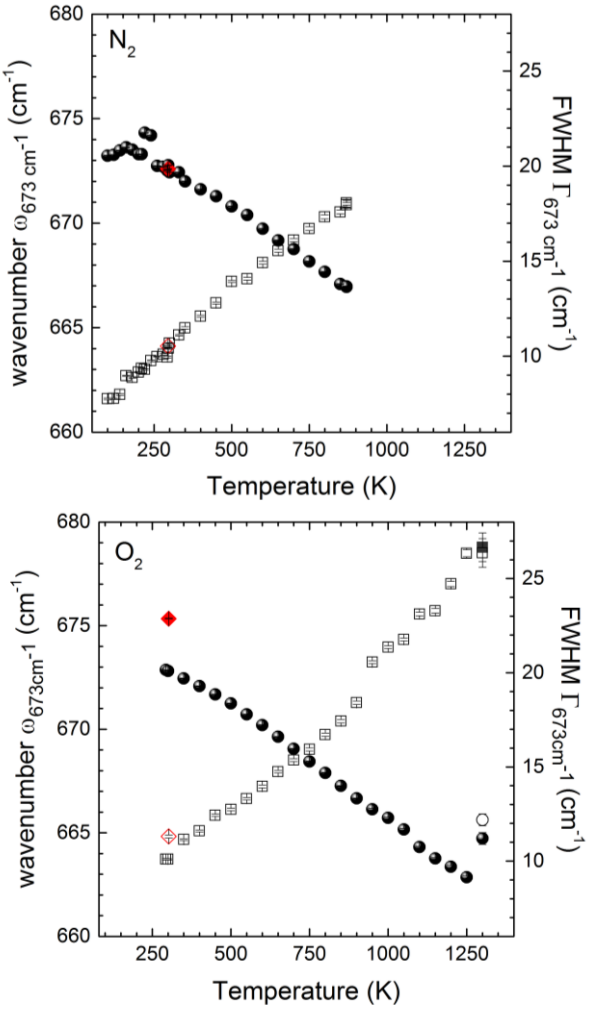

Figure 17: Temperature dependence of phonon wavenumber ω (circles, ●) and FWHM Γ (squares, □) in N_2 and air. The values obtained after the final cooling are displayed by diamonds (♦, ◊). ○ and ■ represent ω and Γ at 1300 K after 30 minutes. If not visible, the error bars are within the symbols.

temperature. In air, $\omega_{673cm^{-1}}$ exhibits a minimum at 1250 K, thus, 50 K after $\omega_{160cm^{-1}}$. This could be indicative for a change in the ring geometry, since the SiO_4-ring has to adapt to the shrinking of the FeO_6 octahedra (Della Ventura et al. 2018). This adaption suggests that the oxidation is irreversible. After cooling down to room temperature the peak appears at higher wavenumbers as initially, which can be explained by the stronger interaction between trivalent iron and its

surroundings. Additionally the FWHM has slightly increased due to the dynamical disorder caused by the heat treatment and/or by oxidation and deprotonation.

The evolution of the fractional intensity I_n of the SiO_4- ring breathing mode cannot be displayed properly by considering only $I_{n\ 673cm^{-1}}$ (Figure 18) because the lower energy shoulder near 655cm^{-1} (peak 16) could not be fitted consistently. By adding $I_{n\ 673cm^{-1}}$ and $I_{n\ 655cm^{-1}}$ (Figure 19) this problem can be solved. Now it is observed that the normalized intensity of the SiO_4-ring breathing mode slightly increases up to 450 K in nitrogen and up to 500 K in air and then slightly decreases towards higher temperatures. In air, the intensity drops off sharply at 1300 K, thus, at the same temperature at which $\omega_{673cm^{-1}}$ is shifted to higher wavenumbers due to the assumed change in the ring geometry. After cooling down to room temperature, the fractional intensity is still reduced. This suggests that the adaption of the SiO_4-ring to the smaller size of Fe^{3+} leads to diminished vibrations in this mode.

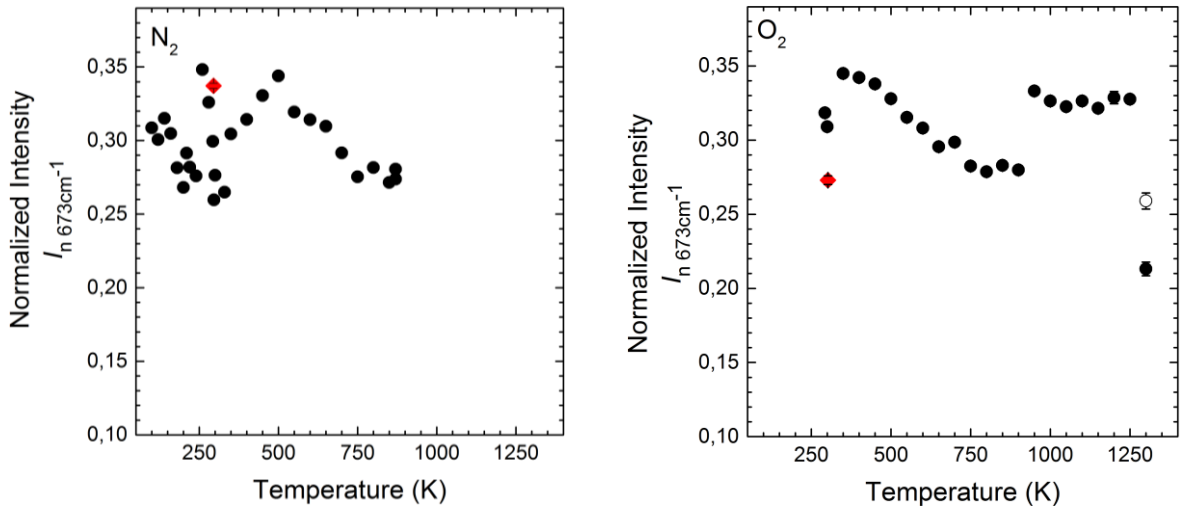

Figure 18: Temperature dependence of $I_{n\ 673cm^{-1}}$ in N_2 and O_2. The symbol code is the same as in Figure 15.

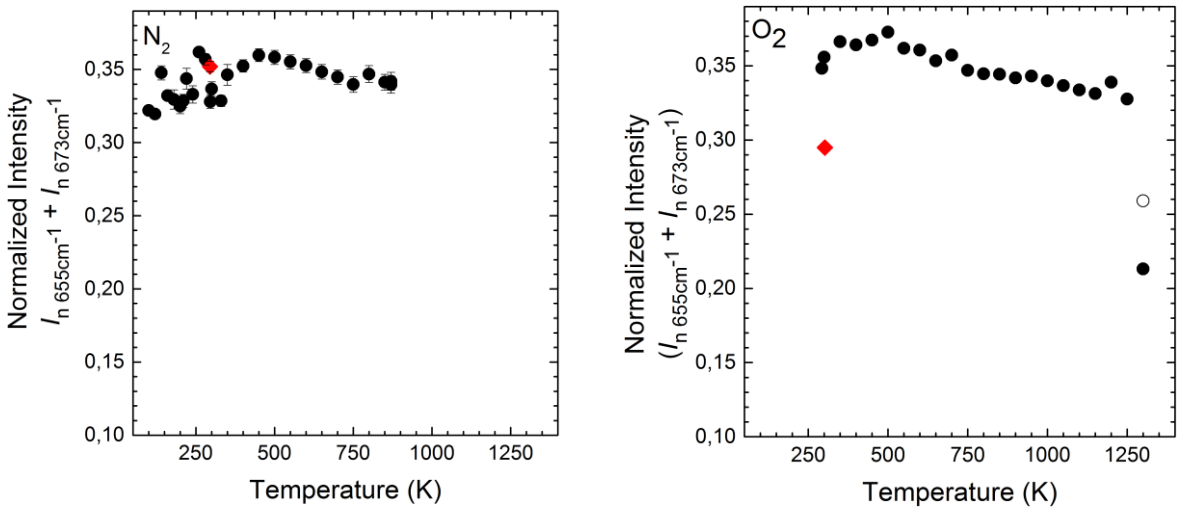

Figure 19: Temperature dependence of $I_{n\ 673cm^{-1}} + I_{n\ 655cm^{-1}}$ in N_2 and O_2. The symbol code is the same as in Figure 15.

Considering all the peaks ascribed to the SiO_4-bending (450-750 cm^{-1}) in the spectrum recorded after cooling to room temperature several changes are observed (Figure 20). New peaks have appeared at ~465 cm^{-1}, ~512 cm^{-1}, ~574 cm^{-1} and ~600 cm^{-1}. The peaks near 482 cm^{-1} (peak 13) and near 564 cm^{-1} (peak 15) cannot be seen anymore. The apparent vanishing of peak 15 may be due to peak overlapping. The fractional intensity of peak 18 (~740 cm^{-1}) has strongly increased. All these changes should be somehow related to the presence of trivalent iron.

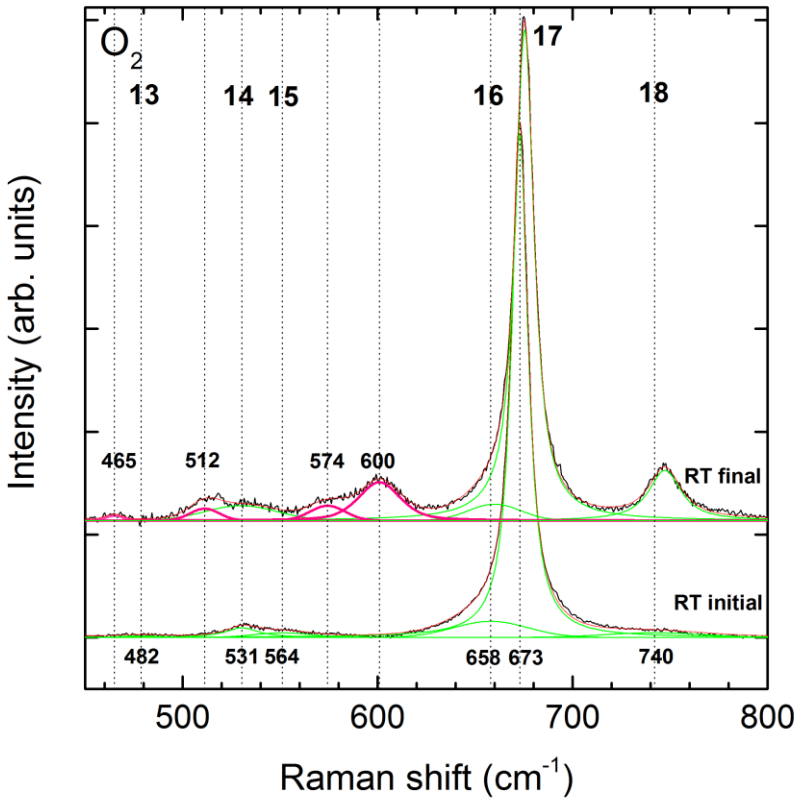

Figure 20: The initial and final Raman spectrum at room temperature in the spectral range from 450-800 cm^{-1}. For the sake of clarity, the spectra have been normalized to the strongest peak in the spectrum (peak 17) and are offset vertically.

3.1.3 The SiO_4 stretching mode

The temperature dependence of the two dominant peaks in the SiO_4 stretching mode (peak 19, ~930 cm^{-1} and peak 22, ~1057 cm^{-1}) in nitrogen and air is displayed in Figure 21. Regarding the peak position ω and the FWHM Γ, peak 19 and peak 22 show the same behaviour on cooling and heating as the peaks discussed so far. With increasing temperature, they gradually shift to lower wavenumbers and get wider. Discontinuities in the FWHM of peak 19 may be caused by unsteady fitting of the overlapping neighbor peak at ~940 cm^{-1} (peak 20). On heating in air the FWHMs start to increase more strongly above 1100 K, indicating a growing dynamical disorder, which should be due to the delocalization of H^+-ions and electrons (Della Ventura et al. 2018). Meanwhile $\omega_{930cm^{-1}}$ reaches a minimum at 1250 K and $\omega_{1057cm^{-1}}$ at 1300 K in the spectrum collected after 5 minutes. After 30 minutes peak 22 is shifted to higher wavenumbers again. As for the peak at ~673 cm^{-1} (peak 17) this minimum in the peak position may indicate a change in the SiO_4-ring geometry as an adjustment for the smaller Fe^{3+} cation (Della Ventura et al. 2018). However, it should be noticed, that above 1200 K the background noise was strongly increased. Therefore, the errors in some peak positions and FWHMs are large. More high temperature

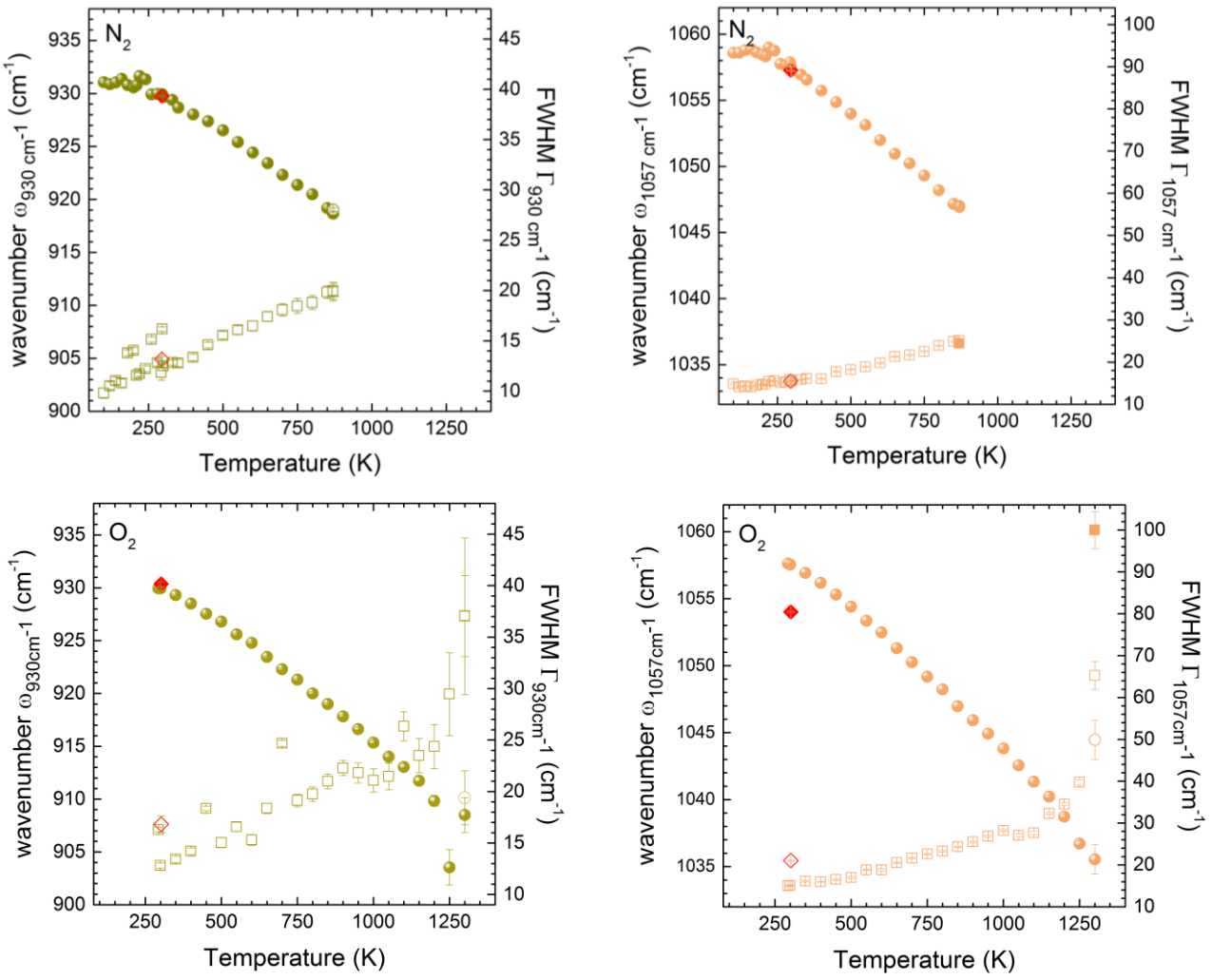

Figure 21: Temperature dependence of phonon wavenumber ω (circles, ●) and FWHM Γ (squares, □) in N_2 and air. The values obtained after the final cooling are displayed by diamonds (♦, ◊). ○ and ■ represent ω and Γ at 870 K in N_2 after 60 minutes and at 1300 K in O_2 after 30 minutes. If not visible the error bars are within the symbols. (a): peak 19 (~930 cm^{-1}), (b): peak 22 (~1057 cm^{-1})

experiments with the same actinolite sample should be made to confirm the observed behavior. After cooling to room temperature peak 19 returns to its initial position, while peak 22 appears shifted to lower wavenumbers. The SiO_4-tetrahedra are sensitive to the occupation at the M(1)M(2)M(3) sites (see the connection in Figure 1). Cations with higher electronegativity are expected to cause a shift to lower wavenumbers in the SiO_4-stretching mode, because they will strengthen the M-O bond in the M-O-Si linkages and hence weaken the O-Si bond. Therefore the observed shift of peak 22 should be indicative for the presence of Fe^{3+} at the C-site.
The fractional intensity of peak 19 slightly decreases with increasing temperature, while the fractional intensity of peak 22 increases (Figure 22). Above 1200 K $I_{n\ 930\ cm^{-1}}$ increases slightly, $I_{n\ 1057cm^{-1}}$ strongly. These intensified vibrations may be due to the delocalization of H^+-ions and electrons.

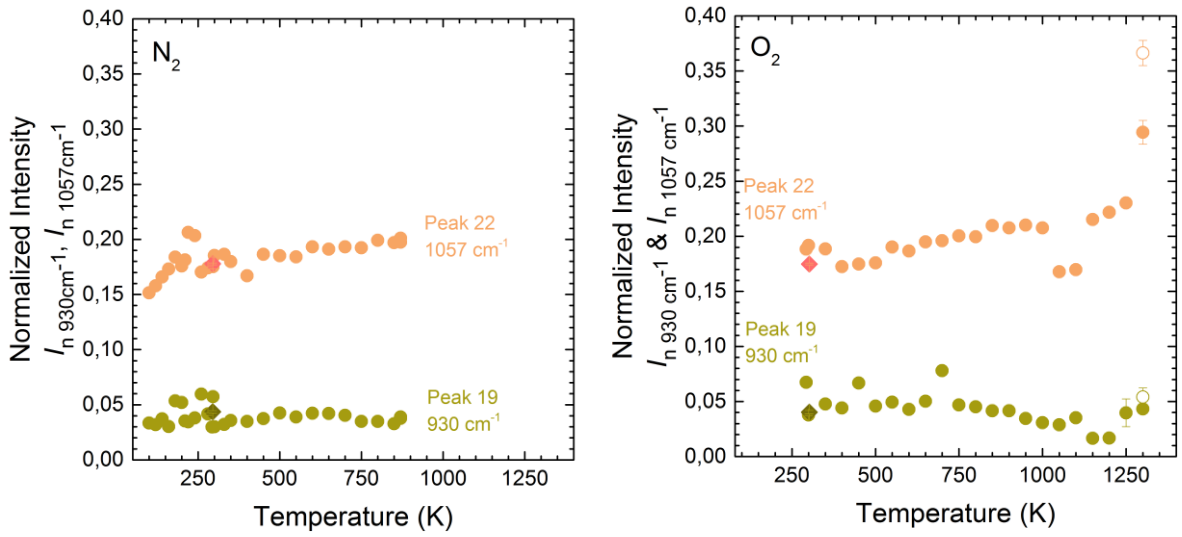

Figure 22: Temperature dependence of $I_{n\ 930\ cm^{-1}}$ and $I_{n\ 1057cm^{-1}}$ in N_2 and O_2. The symbol code is the same as in Figure 15.

Considering the whole spectral range where the SiO_4 stretching vibrations are active, two new peaks are observed in the final spectrum at room temperature (Figure 23) at ~897 cm^{-1} and near 1170 cm^{-1}. The peak at ~897 cm^{-1} possibly can be seen also in the initial spectrum, but it was not fitted because of its weak intensity. A similar peak is observed by Apopei and Buzgar (2010) at 891 cm^{-1} and 892 cm^{-1} in two actinolite samples that are supposed to contain only divalent iron. Therefore it may be enhanced in intensity but not generated by the presence of trivalent iron in the crystal. The new peak near 1170 cm^{-1} in contrast is likely to be generated by the presence of Fe^{3+}, since it is observed neither in the initial spectra recorded in this study, nor in Raman spectra of other Fe^{3+} free actinolite samples found in literature. However, it is also possible that it arises from photoluminescence and therefore the sample should be re-examined by a laser with another wavelength.

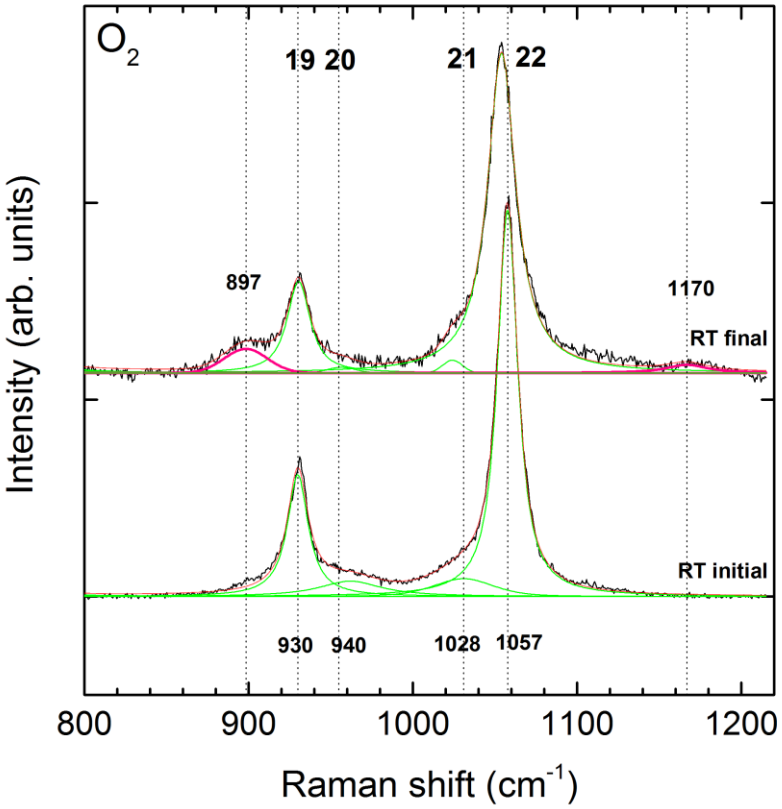

Figure 23: Initial and final Raman spectrum at room temperature in the spectral range from 800-1200 cm^{-1}. For the sake of clarity, the spectra have been normalized to the strongest peak in the spectrum (peak 17) and are offset vertically.

3.2 Raman scattering of the O-H bond stretching mode:

The O-H bond stretching vibrations are strongly influenced by the chemical composition of the C-site since each OH-group shares O with one $M(1)O_6$-$M(1)O_6$-$M(3)O_6$ octahedra triplet (see Figure 1). Moreover the occupancy of the A-site and B(M(4))-site should have an influence on the O-H bond stretching (Leissner et al. 2015).

Figure 24 shows the range from 3570-3770 cm^{-1}, where three sharp peaks appear. In amphiboles with space group *C*2/*m* and Mg^{2+} and Fe^{2+} at the C-site and vacant A-site may occur up to four peaks in this range depending on the Mg^{2+}/Fe^{2+} ratio. Each peak can be related to one of the possible chemical configurations at the M(1)M(1)M(3) sites that are MgMgMg, FeMgMg, FeFeMg and FeFeFe (Burns and Strens 1966). The nomenclature FeMgMg also represents MgFeMg and MgMgFe and the designation FeFeMg includes MgFeFe and FeMgFe. The electronegativity of Fe^{2+} is higher than the electronegativity of Mg^{2+}, which leads to strengthening of the cation-oxygen interaction within the MO_6 octahedron. In return, the O-H bond strength decreases. Hence, the OH-stretching peaks related to iron containing M(1)M(1)M(3) sites appear shifted to lower wavenumbers.

In the Raman spectrum of the studied actinolite sample the peak at 3673 cm^{-1} is assigned to the configuration MgMgMg, the one at 3659 cm^{-1} to Fe^{2+}MgMg and the peak at 3644 cm^{-1} to $Fe^{2+}Fe^{2+}$Mg. A peak corresponding to $Fe^{2+}Fe^{2+}Fe^{2+}$-OH is not observed (Figure 24).

A broad fourth peak arises near 3717 cm^{-1}, due to the influence of the partly filled A-site ($^{A}(Na^{+}_{0,16}K^{+}_{0,01})$) on the vibration of the O-H bonds. Since ^{W}OH–A-cation–^{W}OH species are expected to be observed shifted by ~60 cm^{-1} toward higher wavenumbers with respect to the ^{W}OH–A-vacancy–^{W}OH species (Leissner et al. 2015), this peak should be assigned to the configuration Fe^{2+}MgMg–OH–A-site.

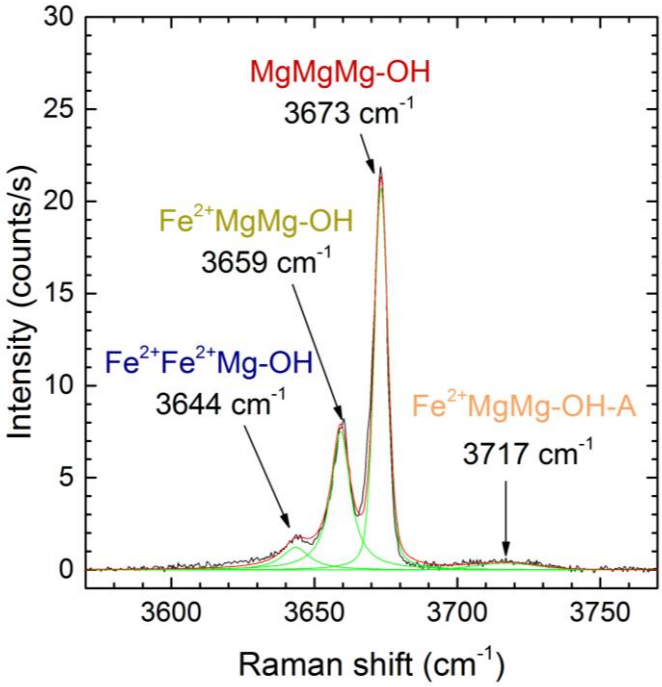

Figure 24: Fitting and peak labelling of the OH-stretching range.

According to Leissner et al. (2015) the content of magnesium and divalent iron at the C-site can be calculated with:

$$Mg^*_{Raman} = \frac{3^*I_{MMM} + 2^*I_{FMM} + I_{FFM}}{3^*I_{MMM} + 3^*I_{FMM} + 3^*I_{FFM} + 3*I_{FFF}}$$

and

$$Fe^{2+}{}^*_{Raman} = 1 - Mg^*_{Raman}$$

where I_{MMM} is the fractional intensity of the MgMgMg peak, I_{FMM} = fractional intensity of Fe^{2+}MgMg peak, I_{FFM} = fractional intensity of the $Fe^{2+}Fe^{2+}$Mg peak and I_{FFF} = fractional intensity of the $Fe^{2+}Fe^{2+}Fe^{2+}$ peak.
Assuming that Mg and Fe^{2+} randomly occupy the M(1), M(2) and M(3) sites, the amount of Mg and Fe^{2+} occupying the C-site calculated with the fractional Raman intensities can be compared to the result obtained by electron microprobe analysis (EMPA) with (Leissner et al. 2015):

$$Mg^*_{EMP} = \frac{{}^{C}Mg}{{}^{C}(Mg + Fe^{2+})}$$

and

$$Fe^{2+}{}^*_{EMP} = \frac{{}^{C}Fe^{2+}}{{}^{C}(Mg + Fe^{2+})}$$

Following this procedure the C-site content of Mg and Fe^{2+} of the studied actinolite sample was calculated using the fractional intensities obtained from the fitting of the initial spectrum recorded at room temperature in air. The uncertainties in the Mg^*_{Raman} and $Fe^{2+}{}_{Raman}$ values were calculated from the errors in the fractional intensities originating from the fittings. The values obtained from the fractional Raman intensities are in good agreement with the EMPA values (Table 5).

Table 5: C-site Mg and Fe^{2+} calculated from EMPA and fractional Raman intensities.

Mg^*_{EMP}	Mg^*_{Raman}	$Fe^{2+}{}^*_{EMP}$	$Fe^{2+}{}^*_{Raman}$
0.891	0.815 ± 0.097	0.109	0.185 ± 0.097

It was considered if also the influence that B-site cations have on the O-H bond vibrations could be observed. According to calculations based on electron microprobe analysis data the B-site of the actinolite sample used in this study is occupied by 1.74 apfu Ca^{2+}, 0.24 apfu Fe^{2+} and 0.02 apfu Mn^{2+} (Leissner 2014). Fe^{2+} and Mn^{2+} are too similar regarding their outermost electron shells and ionic radii to be distinguished from each other. Therefore, in the following when speaking of $^{B}Fe^{2+}$, $^{B}Mn^{2+}$ is included. It was considered if it can be distinguished between the vibrations arising from $^{B}Ca^{2+}$-M1M1M3-OH and $^{B}Fe^{2+}$-M1M1M3-OH linkages. Assuming that there is a subtle peak splitting some spectra were fitted with two additional peaks located at ~3653 cm^{-1} and ~3668 cm^{-1} (Figure 25) representing the B-site Fe^{2+} influence. If these peaks are true it should be possible to calculate the distribution of Ca^{2+} and Fe^{2+} on the B-site (Leissner 2014). Therefore, the percentage of the fractional intensities of the higher and the lower peak was determined. In the Raman spectrum recorded at room temperature the $MgMgFe^{2+}$-OH peak

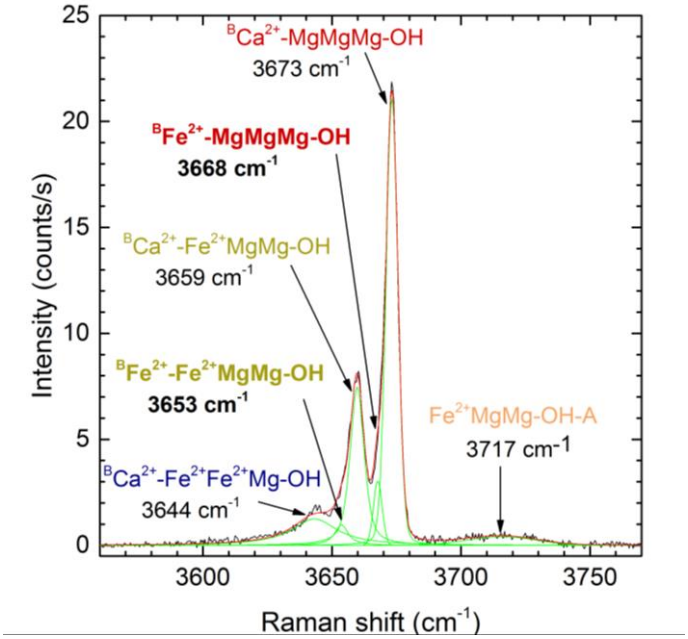

Figure 25: Peak fitting of the OH-stretching mode with two additional peaks (labeled with bold letters).

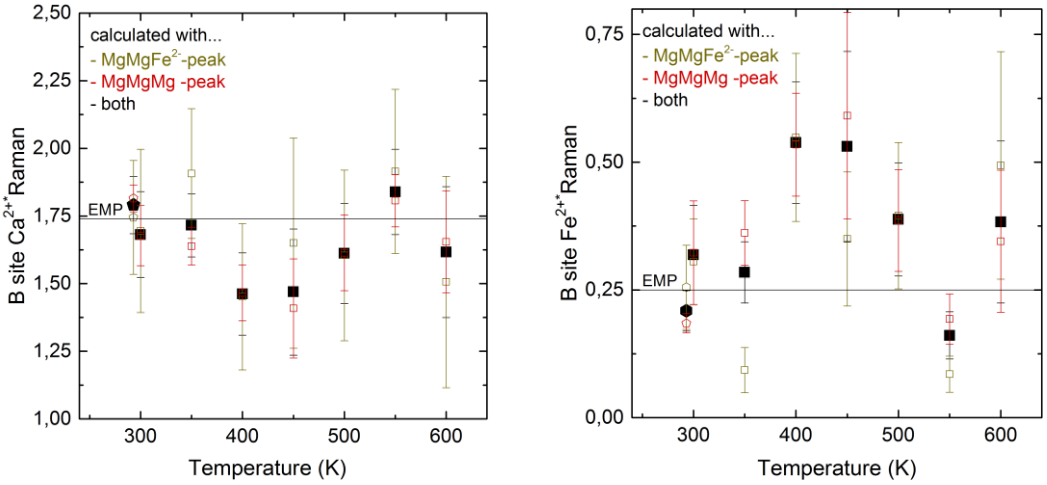

Figure 26: B-site Ca^{2+} and Fe^{2+} content calculated with the normalized Raman intensities of the MgMgMg and $MgMgFe^{2+}$ peaks compared to the electron microprobe values (EMP).

is composed of 12.8 % lower peak (B-site Fe^{2+}) and 87.2 % higher peak (B-site Ca^{2+}). This gives 0.255 apfu Fe^{2+} and 1.745 apfu Ca^{2+} what almost perfectly matches the electron microprobe analysis calculations. For the MgMgMg-OH peak the calculation gives 0.18 apfu Fe^{2+} and 1.82 apfu Ca^{2+}. Here the results do not fit so well the electron microprobe data. Calculations were made for spectra at various temperatures to check if there can be seen any trend. The results are shown in Figure 26.

Although some values match the theory of peak splitting due to B-site influence the overall results do not show evidence that the additional lower peaks are true. To avoid overinterpretation of the data the spectra fitted without the additional peaks were used in this study.

3.2.1 Temperature dependence of phonon wavenumbers, widths and fractional intensities of the OH-stretching mode

The temperature dependence of the phonon wavenumbers ω and FWHMs Γ is displayed in Figure 28 and Figure 29. For every peak the peaks position ω gradually shifts to lower wavenumbers with increasing temperatures while the peaks become broader. This shows that also the O-H bonds get weaker and the dynamical disorder increases during the heat treatment.

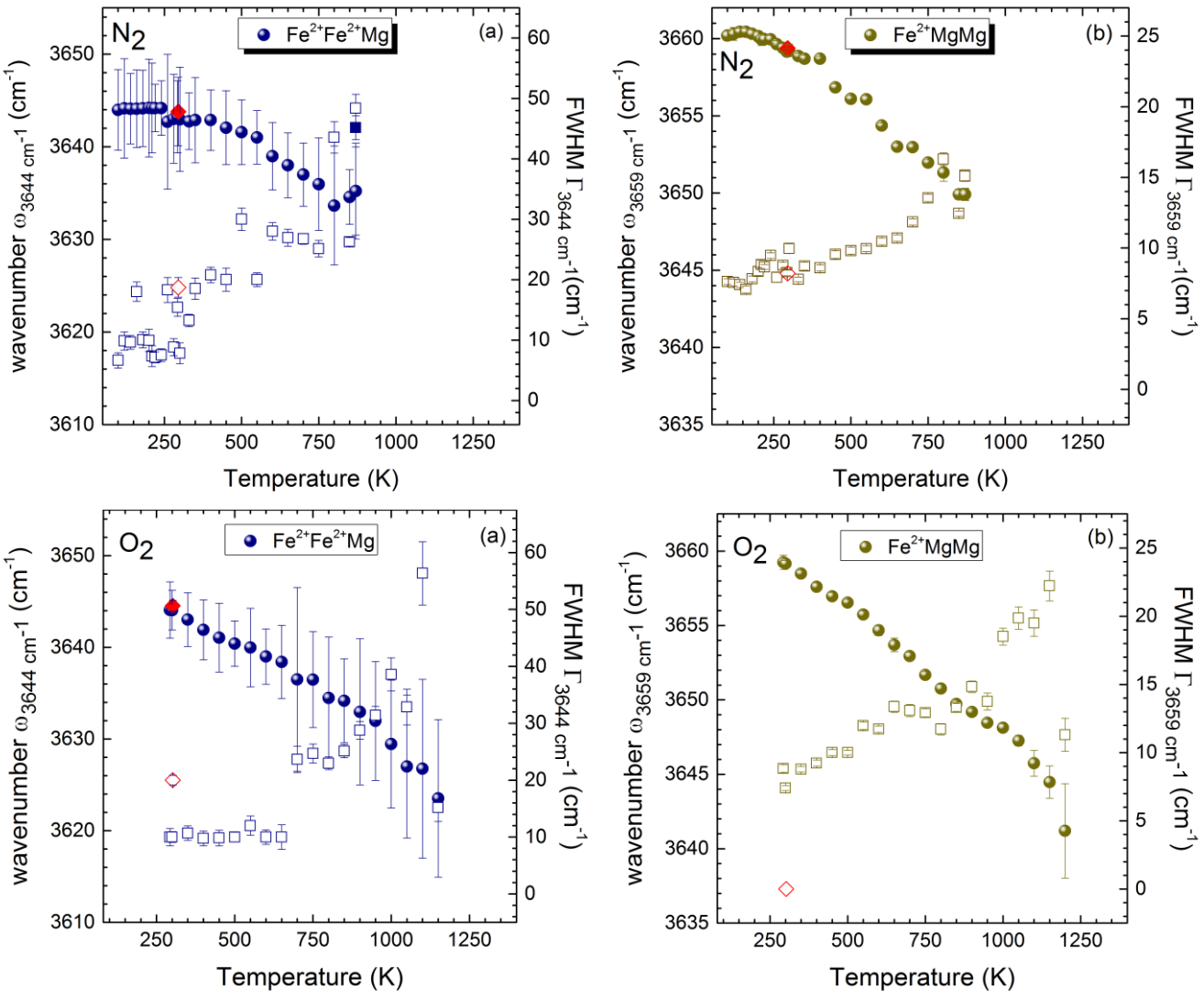

Figure 28: Temperature dependence of phonon wavenumbers ω and FWHMs Γ in N_2 and O_2 of the peaks near 3673 cm^{-1} (a), 3659 cm^{-1} (b). The symbol code is the same as in Figure 14.

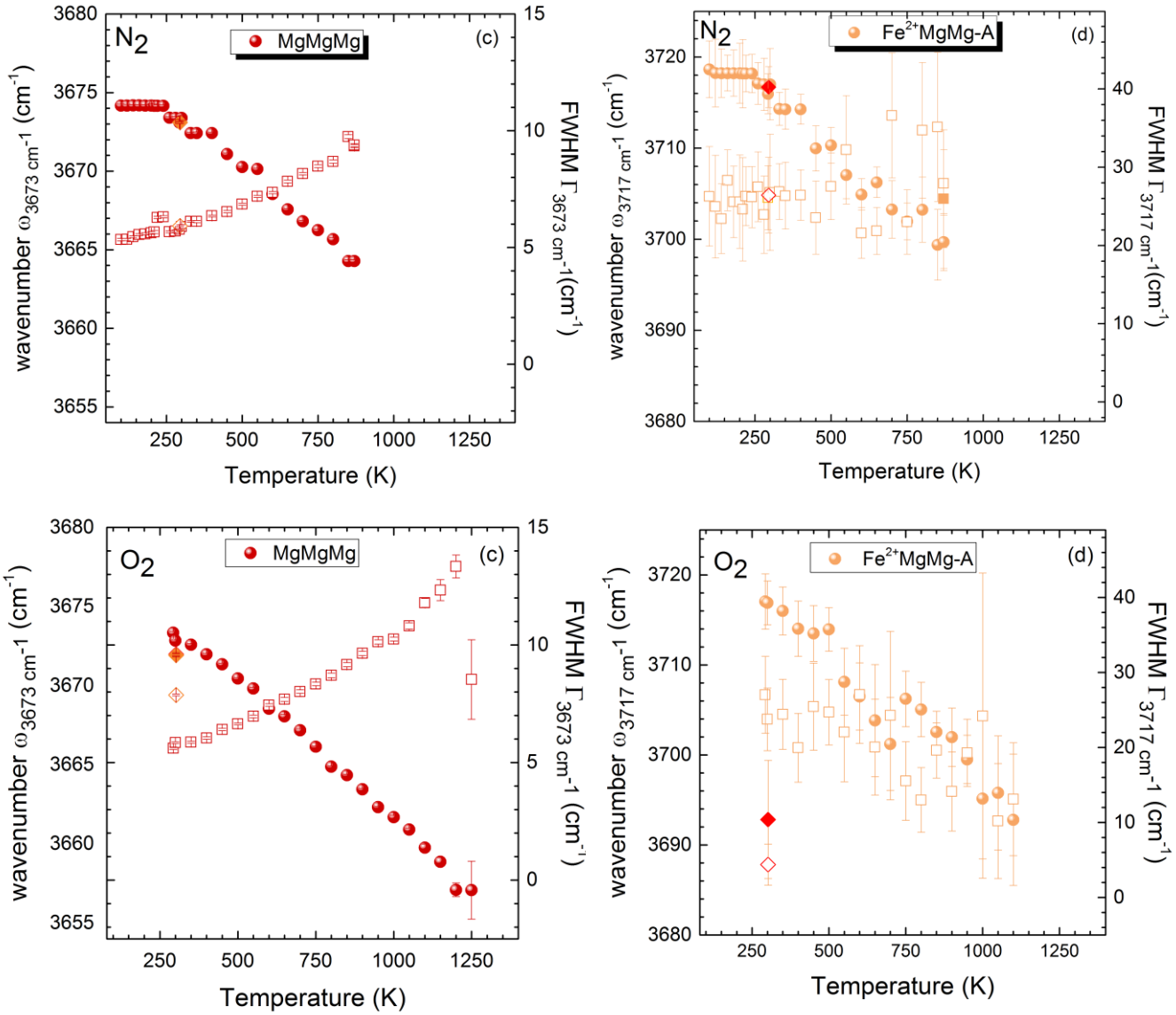

Figure 29: Temperature dependence of phonon wavenumbers ω and FWHMs Γ in N_2 and O_2 of the peaks near 3644 cm^{-1} (c) and 3717 cm^{-1} (d). The symbol code is the same as in Figure 14.

The fractional intensities of the OH-stretching peaks barely change when heating in nitrogen (Figure 30). On heating in air in contrast can be observed that something is changing (Figure 31). Above 1150 K the peaks disappear one after the other. At 1300 K no signal form the O-H bonds is measured anymore. About 100 K before vanishing the FWHMs of all the peaks assigned to the M(1)M(1)M(3) sites and the intensities of the FeFeMg- and FeMgMg-peak normalized to the intensity of the framework vibrations reach their maximum, which indicates the onset of H^+ delocalization (Della Ventura et al. 2018). Apparently hydrogen cations related to the FeFeMg triplets start to delocalize at 1100 K, that related to the FeMgMg triplets at 1150 K and that related to the MgMgMg triplets at 1200 K. This shows that the ease with that H^+ cations delocalize depends on the Fe content at the M(1)M(1)M(3) sites. Since the electronegativity of iron is higher than the electronegativity of magnesium, Fe^{2+} cations bond stronger to the surrounding oxygen atoms, which weakens the O-H bonds.

After cooling down to room temperature, the fractional intensities of the MgMgMg-peak and the $Fe^{2+}Fe^{2+}Mg$ peaks are increased compared to the initial intensities, the $Fe^{2+}MgMg$-A site peak appears with a decreased intensity and the $Fe^{2+}MgMg$ peak near 3659 cm^{-1} can not be seen anymore. This partial recovery can be explained by following the idea that the dehydroxylation reaction in Fe-bearing amphiboles proceeds in different steps. According to this, when heating up to 1300 K all electrons and hydrogen cations in the studied actnolite sample are delocalized but only some have left the crystal.

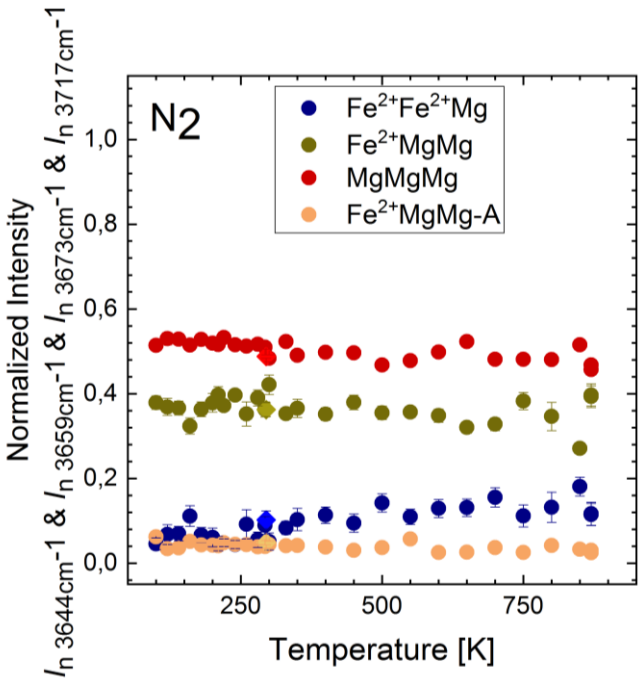

Figure 30: Temperature dependence of the intensity of each OH-stretching peak normalized to the total intensity of the OH-stretching vibrations in N_2. The symbol code is the same as in Figure 15.

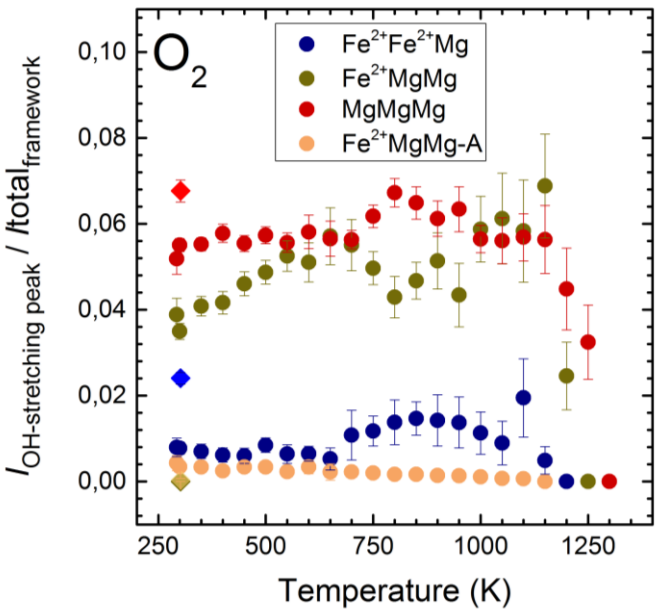

Figure 31: Temperature dependence of intensity of each OH-stretching peak normalized to the total intensity of the framework vibrations in O_2. The symbol code is the same as in Figure 15.

3.2.2 Final spectrum after heating in O_2

In the spectrum recorded finally after the heat treatment it is remarkable that near 3659 cm^{-1} no peak can be seen anymore (Figure 32). Thus, no vibration from Fe^{2+}MgMg-OH bonds is observed. The peak related to the $Fe^{2+}Fe^{2+}$Mg-triplet (~3644 cm^{-1}) is still present but has become broader and its intensity has increased. The peak associated with the MgMgMg-triplet (~3673 cm^{-1}) has broadened slightly. The peak arisen by the vibration of the Fe^{2+}MgMg-OH–A-site linkage (~3717 cm^{-1}) appears strongly shifted to lower wavenumbers at ~3693 cm^{-1} with a decreased FWHM and intensity. This shift to lower wavenumbers can be explained by the

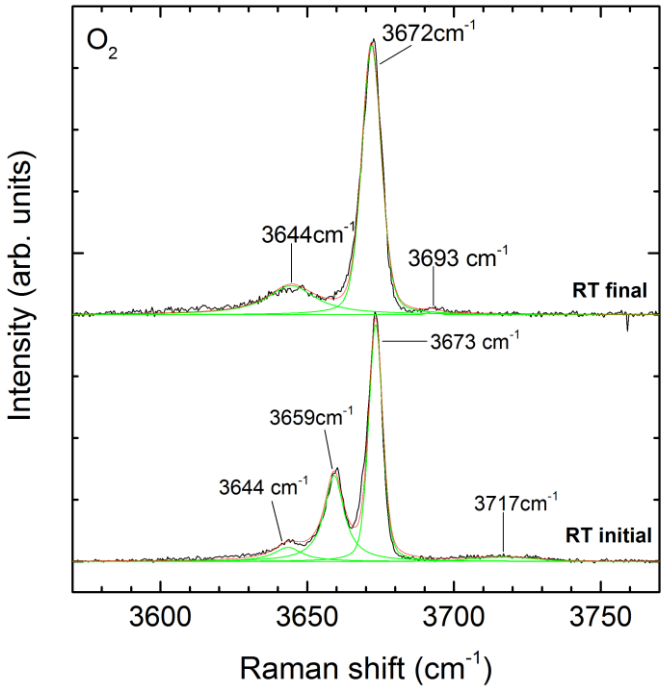

Figure 32: Initial and final Rama spectrum at room temperature in the range from 3570-3770 cm^{-1}. For the sake of clarity, the spectra have been normalized to the intensity of the strongest peak in the spectrum (peak 17) and are offset vertically.

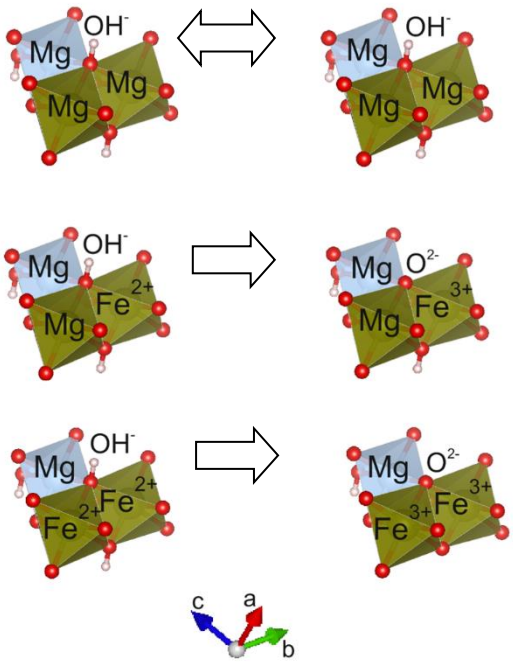

Figure 33: Different local configurations at the M1M1M3 triplet before (left) and after (right) oxidation. Olive green: M(1) octahedra, light blue: M(3) octahedra. This figure was prepared using the VESTA software package (Momma and Izumi 2008). (Color online)

change of the chemical configuration to Fe^{3+}MgMg–A-site with two $^{W}OH^{-}$ instead of three (Figure 33). When Fe^{2+} is replaced by Fe^{3+} in the M(1)M(1)M(3)–A-site species, the stronger M(1),M(3)-O_6 interaction leads to weakening of the O-H bonds. The decrease in intensity should be due to the reduced amount of OH- groups. The same logic can be applied to the Fe^{2+}MgMg-$^{A}\square$ configuration. When it is changed to Fe^{3+}MgMg–$^{A}\square$, the corresponding peak should appear at lower wavenumbers with a decreased intensity. This would explain the increased intensity and the strong broadening of the peak near 3644 cm^{-1}. It is most probable composed of two components: one corresponding to the chemical configuration $Fe^{2+}Fe^{2+}$Mg–$^{A}\square$, which should not have changed, and the other corresponding to the configuration Fe^{3+}MgMg-$^{A}\square$. According to this, the oxidation of M(1)M(1)M(3) species containing only one Fe^{2+} cation happens before the oxidation of those containing two Fe^{2+} cations.

In Table 6 these assumptions are listed. Furthermore the percentage decrease of the fractional intensities was calculated. According to the calculations, the FeMgMg–^{A}□ peak is reduced by ~53 % and the FeMgMg–A-site peak by ~90 %. This difference could be explained as follows: OH-groups prefer to be next to A-site vacant M(1)M(1)M(3) species for having more space. Therefore H^{+} cations of OH-groups attached to M(1)M(1)M(3) sites next to filled A-sites should be preferentially ejected first.

Table 6: Chemical configurations and fractional intensities of the peaks near 3644 cm^{-1}, 3659 cm^{-1} and 3717 cm^{-1} before and after the heat treatment. The fractional intensities I_n are the intensities obtained from the fittings normalized to the area of the whole OH-stretching region.

Initial chemical configuration and wavenumber	**$Fe^{2+}Fe^{2+}Mg–^{A}$□** ~3644 cm^{-1}	**$Fe^{2+}MgMg–^{A}$□** ~3659 cm^{-1}	**Fe^{2+}MgMg–A-site** 3717 cm^{-1}
Final chemical configuration and wavenumber	$Fe^{2+}Fe^{2+}Mg–^{A}$□ ~3644 cm^{-1}	$Fe^{3+}MgMg–^{A}$□ < 3659 cm^{-1}	Fe^{3+}MgMg–A-site 3693 cm^{-1}
I_n initial	~0.08	~0.38	~0.042
I_n final	from peak fit: ~0.26 should be: ~0.08	~0.26 - ~0.08 ≈ 0.18	~0.004
I_n decrease (%)	should not change	$1 - \frac{0.18}{0.38} \approx 0.526$ ⇨ **~53 %**	$1 - \frac{0.004}{0.042} \approx 0.905$ ⇨ **~90 %**

Following the idea that the amount of oxidized iron at different temperatures could be determined by using the fractional intensities, the $Fe^{2+}*_{Raman}$ ratio was calculated for increasing temperatures applying the procedure discussed earlier. The results are presented in Figure 34. Unfortunately the errors are too large to allow any assumptions. The value obtained from the intensities in the final spectrum lies within the error of the initial $Fe^{2+}{}_{Raman}$ ratio. Since the observed changes in the spectra indicate that iron has been oxidized, the content of Fe^{2+} should have decreased.

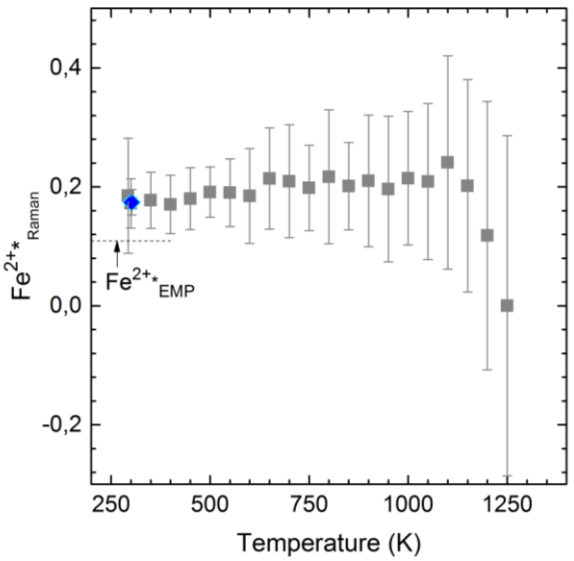

Figure 34: The $Fe^{2+}*_{Raman}$ ratio at increasing temperatures (♦ represents the $Fe^{2+}{}_{Raman}$ ratio after the heat treatment).

3.3 Phonon thermal expandability

Since all the peak positions show a linear temperature dependence (see e.g. Figure 14) $\omega(T) = \omega_0 + (d\omega/dT)T$, the phonon thermal expandability $\alpha_\omega = (d\omega/dT)/\omega_0$ for each phonon can be calculated from the linear curve fit of $\omega(T)$ (Watenphul et al. 2017). The phonon thermal expandability α_ω in actinolite was calculated for several framework peaks and for the peaks in the OH-stretching mode. The values obtained for α_ω were plotted against the phonon wavenumbers (Figure 35). Due to the discontinuities at low temperatures in nitrogen the phonon thermal expandability was determined for the temperature range from 300 K to 850 K. For better comparison also in air only the temperature range from 300 K to 850 K was considered. The data show that the thermal expansion of phonons observed at lower wavenumbers is larger than the thermal expansion of phonons observed at higher wavenumbers. The chemical entities that are the most resistant to temperature increase are the O-H bonds, followed by the SiO_4-ring, which is more temperature resistant than the individual SiO_4-tetrahedra. The octahedral modes are least resistant to increasing temperatures. The phonon thermal expandability in O_2 compared to that in N_2 reveals that the dynamic instability of the structure is higher when heating in air. The largest deviation exhibits peak 1 (120 cm^{-1}), which, as discussed in chapter 3.1.1, disappears at temperatures above 1150 K and does not recover when cooling down again. Both indicates that this peak is very sensitive to temperature-induced changes within the crystal.

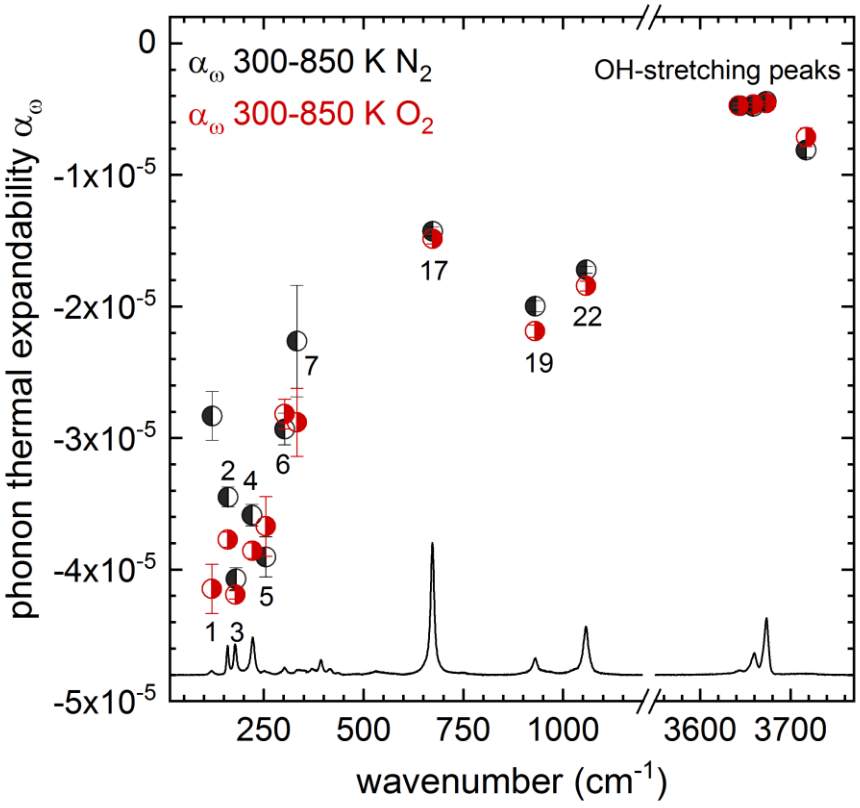

Figure 35: The phonon thermal expandability α_ω calculated for several phonons in N_2 and O_2

4 Conclusions

This study shows the thermal behavior of phonons in actinolite at temperatures from 100 K to 870 K in nitrogen and from room temperature to 1300 K in air. In general, actinolite shows the behavior expected for a material with a positive thermal expansion: with increasing temperature, the chemical bonds weaken and the phonon decay increases. The calculated phonon thermal expandability shows that the O-H bonds are the most resistant to temperature increase, followed by the SiO_4-ring, then the SiO_4 tetrahedra and last the octahedral modes. Furthermore it is revealed that the dynamic instability of the structure is higher in air than in N_2.

On cooling in N_2, an anomaly in the trend of all peak positions is observed: below 160 K, the peaks gradually shift back to lower wavenumbers. There is no sound explanation yet. Further studies should be made examining amphiboles at low temperatures.

Differences that could be observed between heating in nitrogen and air mainly concern the development of the total intensity of the vibrational modes in the crystal. In N_2 the total intensity barely changes while in air it decreases up to 600 K and then increases on further heating to 850 K before decreasing strongly at higher temperatures. Since in this study temperatures higher than 870 K have not been reached in N_2, the temperature range above cannot be compared. All changes emerging on heating in nitrogen are reversible upon cooling to room temperature. After the heat treatment in air in contrast the sample appears irreversibly altered.

On heating in air, the evolution of the intensities in the OH-stretching range indicates that the delocalization of hydrogen cations starts at 1100 K. At 1300 K no signal from the OH-stretching peaks is observed anymore, which implies that all H^+ cations are delocalized at that temperature. When cooling down to room temperature, a partial recovery of the OH-stretching peaks is observed. This indicates that only some delocalized hydrogen cations have been ejected from the crystal and the others have rebonded. Thus, the temperature of complete dehydroxylation of actinolite at atmospheric pressure lies above 1300 K. To determine the temperature of total dehydroxylation another study with the same actinolite sample should be made.

Several features in the spectrum recorded finally at room temperature indicate that some divalent iron has be oxidized to trivalent iron. The stronger interaction of Fe^{3+} with its environment strengthens the bonds within the $Fe^{3+}O_6$ octahedra while other interactions weaken. This is revealed by the shift of the peaks arisen from octahedral MO_6 vibrations to higher wavenumbers and the shift of the SiO_4-stretching peak at 1057 cm^{-1} to lower wavenumbers. Moreover the peaks associated with the chemical configurations $Fe^{2+}MgMg–^{A}\square$ and $Fe^{2+}MgMg–$A-site appear strongly shifted to lower wavenumbers with a decreased intensity, which indicates that the configurations have changed to $Fe^{3+}MgMg–^{A}\square$ and $Fe^{3+}MgMg–$A-site. The peak related to the $Fe^{2+}Fe^{2+}Mg$-triplets is observed at its initial position. Therefore it is assumed that only divalent iron located at $Fe^{2+}MgMg$-triplets has been oxidized. Furthermore, the MO_6 and SiO_4-ring geometry has slightly changed to adapt to the smaller size of the Fe^{3+}-cations. This is indicated by a minimum in the peak position of the peak at ~160 cm^{-1} at 1200 K and of the peak at ~637 cm^{-1} at 1250 K. In the final spectrum at room temperature the peaks appear at higher wavenumbers. New peaks are observed near 292 cm^{-1}, 465 cm^{-1}, 512 cm^{-1}, 574 cm^{-1}, 600 cm^{-1}, 897 cm^{-1} and 1170 cm^{-1}, whereby the peaks near 292 cm^{-1} and 897 cm^{-1} may be not new but increased in intensity. The new peaks should be indicative for the presence of trivalent iron.

References

Addison, W.E., and Sharp, J.H. (1962) A Mechanism for the Oxidation of Ferrous Iron in Hydroxylated Silicates. Clay Minerals, 5 (28), 73–79.

Apopei, A.I., and Buzgar, N. (2010) The Raman study of amphiboles. Analele Stiintifice de Universitatii AI Cuza din Iasi. Sect. 2, Geologie, 56 (1), 57.

Burns, R.G., and Strens, R.G.J. (1966) Infrared study of the hydroxyl bands in clinoamphiboles. Science (New York, N.Y.), 153 (3738), 890–892.

Cipriani, C. (2007) Amphiboles: historical perspective. Reviews in Mineralogy and Geochemistry, 67 (1), 517–546.

Deer, W.A., Howie, R.A., and Zussman, J. (2013) An introduction to the rock-forming minerals: Mineralogical Society London.

Della Ventura, G., Mihailova, B., Susta, U., Guidi, M.C., Marcelli, A., Schlüter, J., and Oberti, R. (2018) The dynamics of Fe oxidation in riebeckite: A model for amphiboles. American Mineralogist, 103 (7), 1103–1111.

Evans, B.W., and Yang, H. (1998) Fe-Mg order-disorder in tremolite-actinolite-ferro-actinolite at ambient and high temperature. American Mineralogist, 83 (5-6), 458–475.

Ferraro, J.R., Nakamoto, K., and Brown, C.W. (2003) Introductory raman spectroscopy. Academic Press.

Hacker, B.R., Peacock, S.M., Abers, G.A., and Holloway, S.D. (2003) Subduction factory 2. Are intermediate-depth earthquakes in subducting slabs linked to metamorphic dehydration reactions? Journal of Geophysical Research: Solid Earth, 108 (B1).

Hawthorne, F.C., and Oberti, R. (2007) Amphiboles: crystal chemistry. Reviews in Mineralogy and Geochemistry, 67 (1), 1–54.

Hawthorne, F.C., Oberti, R., Harlow, G.E., Maresch, W.V., Martin, R.F., Schumacher, J.C., and Welch, M.D. (2012) Nomenclature of the amphibole supergroup. American Mineralogist, 97 (11-12), 2031–2048.

Ishida, K., Hawthorne, F.C., and Ando, Y. (2002) Fine structure of infrared OH-stretching bands in natural and heat-treated amphiboles of the tremolite-ferro-actinolite series. American Mineralogist, 87 (7), 891–898.

Kakkar, R. (2015) Atomic and Molecular Spectroscopy Cambridge University Press.

Kamp, D.W., Graceffa, P., Pryor, W.A., and Weitzman, S.A. (1992) The role of free radicals in asbestos-induced diseases. Free Radical Biology and Medicine, 12 (4), 293–315.

Klein, C., and Philpotts, A.R. (2012) Earth Materials: Introduction to Mineralogy and Petrology Cambridge University Press.

Kroumova, E., Aroyo, M.I., Perez-Mato, J.M., Kirov, A., Capillas, C., Ivantchev, S., and Wondratschek, H. (2003) Bilbao crystallographic server: useful databases and tools for phase-transition studies. Phase Transitions: A Multinational Journal, 76 (1-2), 155–170.

Leissner, L. (2014) Crystal chemistry of amphiboles studied by Raman spectroscopy. Master thesis in Geoscience.

Leissner, L., Schlüter, J., Horn, I., and Mihailova, B. (2015) Exploring the potential of Raman spectroscopy for crystallochemical analyses of complex hydrous silicates: I. Amphiboles. American Mineralogist, 100 (11-12), 2682–2694.

Li, K., and Xue, D. (2006) Estimation of electronegativity values of elements in different valence states. The Journal of Physical Chemistry A, 110 (39), 11332–11337.

Locock, A.J. (2014) An Excel spreadsheet to classify chemical analyses of amphiboles following the IMA 2012 recommendations. Computers & Geosciences, 62, 1–11.

Momma, K., and Izumi, F. (2008) VESTA: a three-dimensional visualization system for electronic and structural analysis. Journal of Applied Crystallography, 41 (3), 653–658.

Nasdala, L., Smith, D.C., Kaindl, R., and Ziemann, M.A. (2004) Raman spectroscopy: analytical perspectives in mineralogical research. Spectroscopic methods in mineralogy, 6, 281–343.

Oberti, R., Boiocchi, M., Zema, M., Hawthorne, F.C., Redhammer, G.J., Susta, U., and Della Ventura, G. (2018) The high-temperature behaviour of riebeckite: expansivity, deprotonation, selective Fe oxidation and a novel cation disordering scheme for amphiboles. European Journal of Mineralogy, 30 (3), 437–449, DOI: 10.1127/ejm/2018/0030-2712.

Schaller, W.T. (1916) Mineralogic notes series 3. Washington: Government Printing Office.

Schumacher, J.C. (2007) Metamorphic amphiboles: composition and coexistence. Reviews in Mineralogy and Geochemistry, 67 (1), 359–416.

Shukla, A., Gulumian, M., Hei, T.K., Kamp, D., Rahman, Q., and Mossman, B.T. (2003) Multiple roles of oxidants in the pathogenesis of asbestos-induced diseases. Free Radical Biology and Medicine, 34 (9), 1117–1129.

Susta, U., Della Ventura, G., Hawthorne, F.C., Abdu, Y.A., Day, M.C., Mihailova, B., and Oberti, R. (2018) The crystal-chemistry of riebeckite, ideally Na 2 Fe 2+ 3 Fe 3+ 2 Si 8 O 22 (OH) 2: a multi-technique study. Mineralogical Magazine, 1–37.

Tuschel, D. (2014) Practical group theory and Raman spectroscopy, Part I: Normal vibrational modes. Spectroscopy, 29 (2), 14.

Wang, D., Guo, Y., Yu, Y., and Karato, S.-i. (2012) Electrical conductivity of amphibole-bearing rocks: influence of dehydration. Contributions to Mineralogy and Petrology, 164 (1), 17–25.

Watenphul, A., Malcherek, T., Wilke, F.D.H., Schlüter, J., and Mihailova, B. (2017) Composition-thermal expandability relations and oxidation processes in tourmaline studied by in situ Raman spectroscopy. Physics and Chemistry of Minerals, 44 (10), 735–748.

Welch, M.D., and Knight, K.S. (1999) A neutron powder diffraction study of cation ordering in high-temperature synthetic amphiboles. European Journal of Mineralogy, 11 (2), 321–331.

Appendix

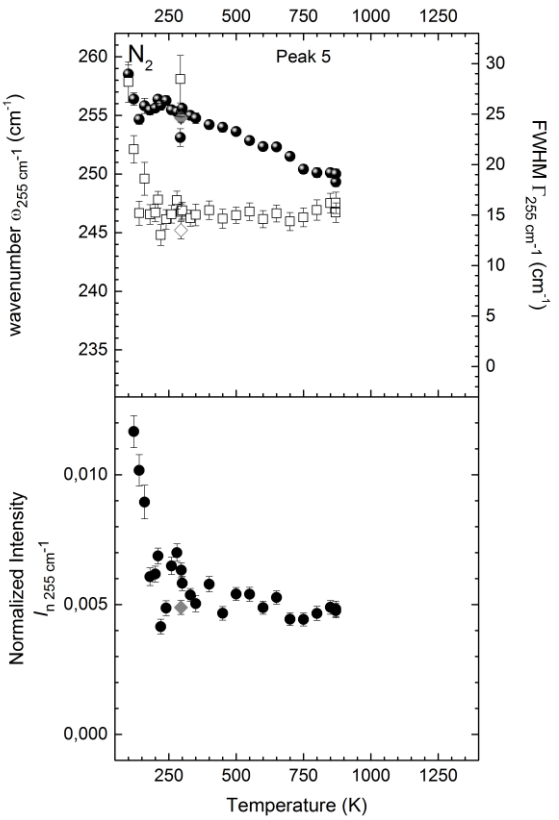
N2
Peak 5
wavenumber ω255 cm-1 (cm-1)
FWHM Γ255 cm-1 (cm-1)
Normalized Intensity
In 255 cm-1
Temperature (K)

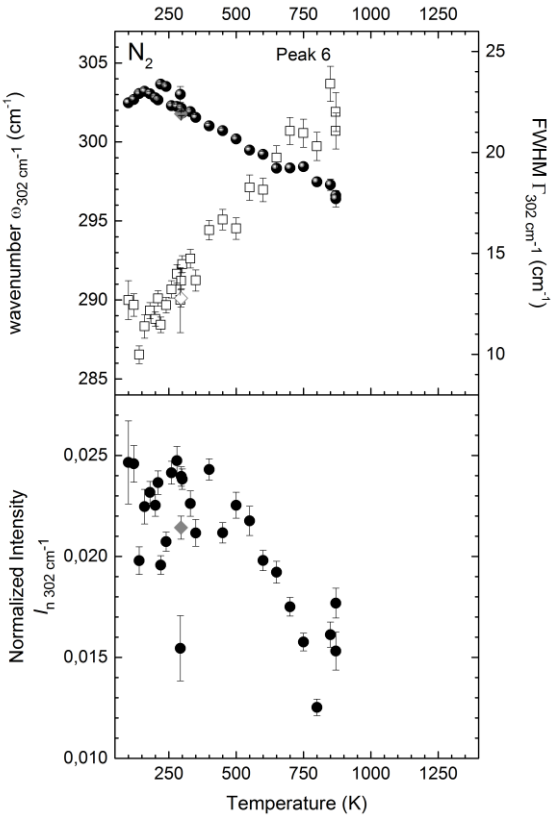
N2
Peak 6
wavenumber ω302 cm-1 (cm-1)
FWHM Γ302 cm-1 (cm-1)
Normalized Intensity
In 302 cm-1
Temperature (K)

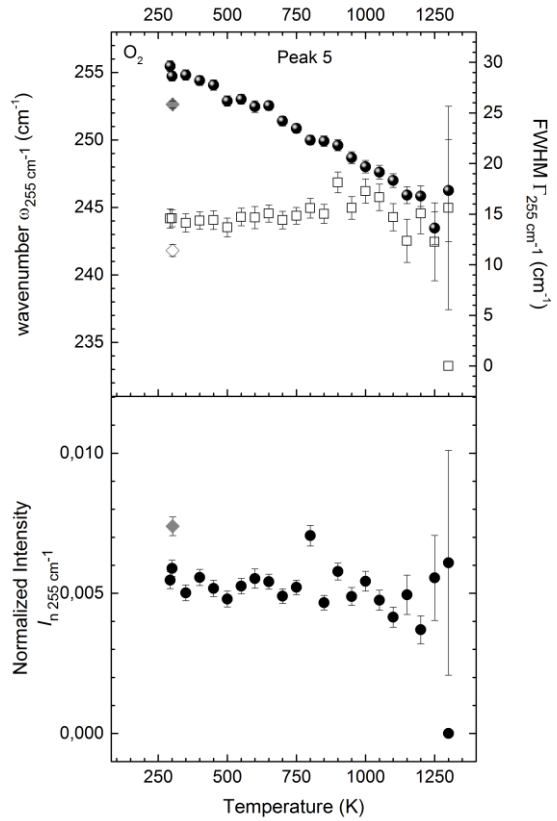
O2
Peak 5
wavenumber ω255 cm-1 (cm-1)
FWHM Γ255 cm-1 (cm-1)
Normalized Intensity
In 255 cm-1
Temperature (K)

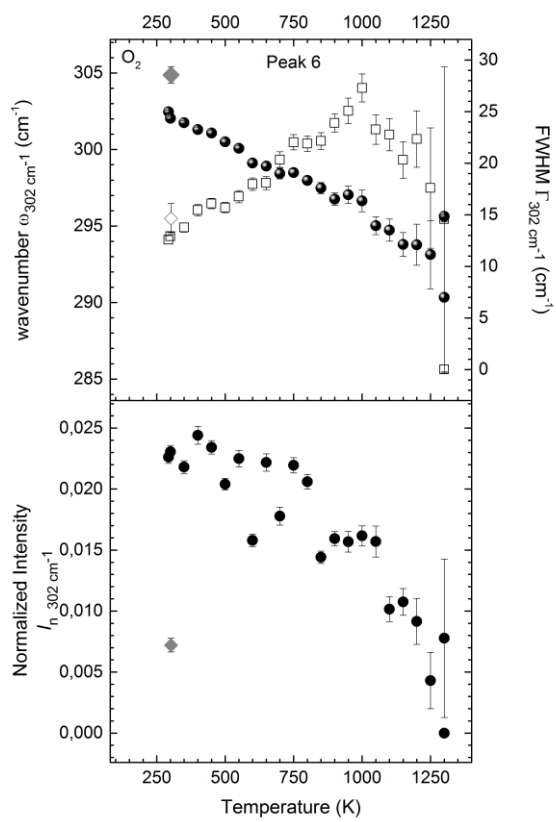
O2
Peak 6
wavenumber ω302 cm-1 (cm-1)
FWHM Γ302 cm-1 (cm-1)
Normalized Intensity
In 302 cm-1
Temperature (K)

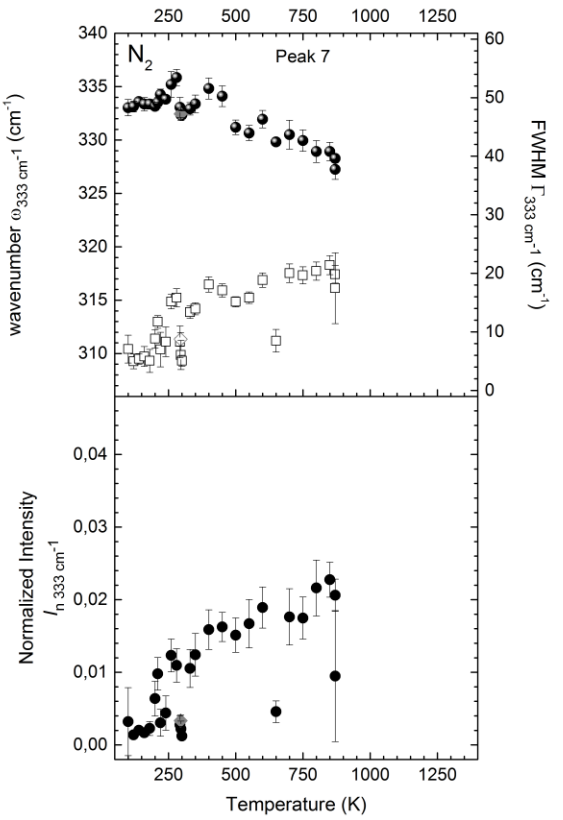
N2
Peak 7
wavenumber ω333 cm-1 (cm-1)
FWHM Γ333 cm-1 (cm-1)
Normalized Intensity
In 333 cm-1
Temperature (K)

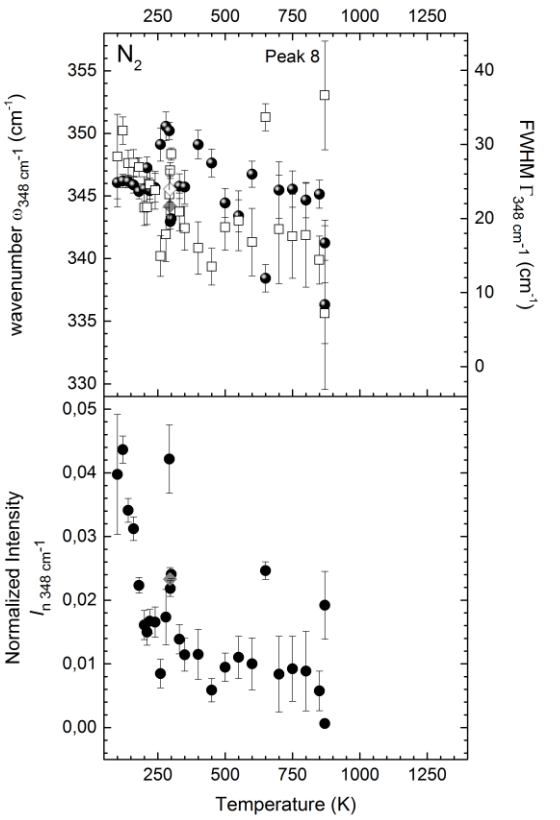
N2
Peak 8
wavenumber ω348 cm-1 (cm-1)
FWHM Γ348 cm-1 (cm-1)
Normalized Intensity
In 348 cm-1
Temperature (K)

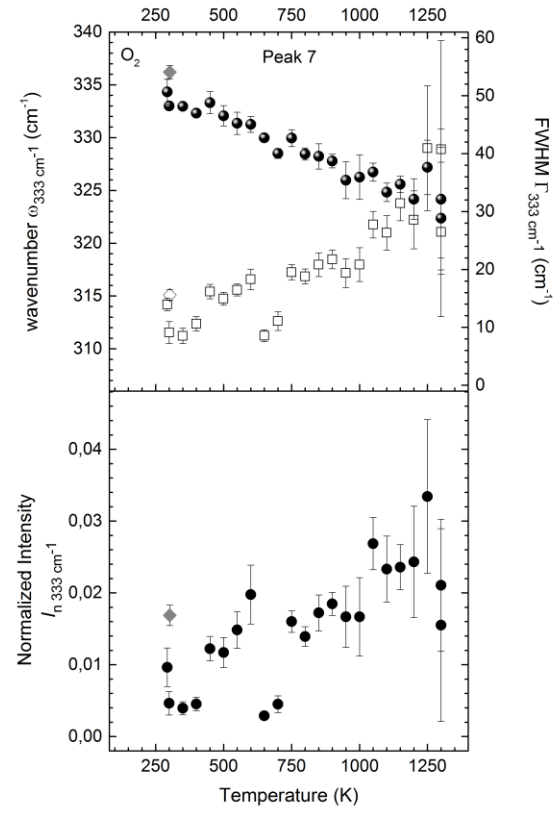
O2
Peak 7
wavenumber ω333 cm-1 (cm-1)
FWHM Γ333 cm-1 (cm-1)
Normalized Intensity
In 333 cm-1
Temperature (K)

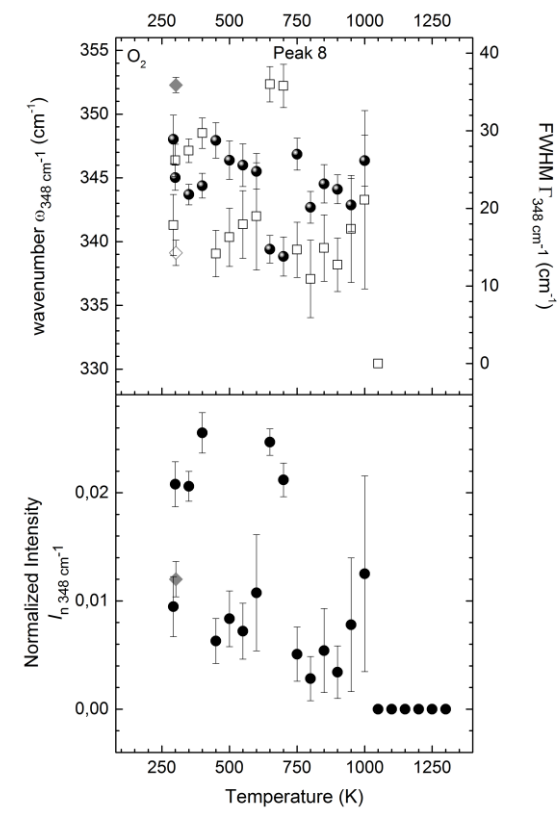
O2
Peak 8
wavenumber ω348 cm-1 (cm-1)
FWHM Γ348 cm-1 (cm-1)
Normalized Intensity
In 348 cm-1
Temperature (K)

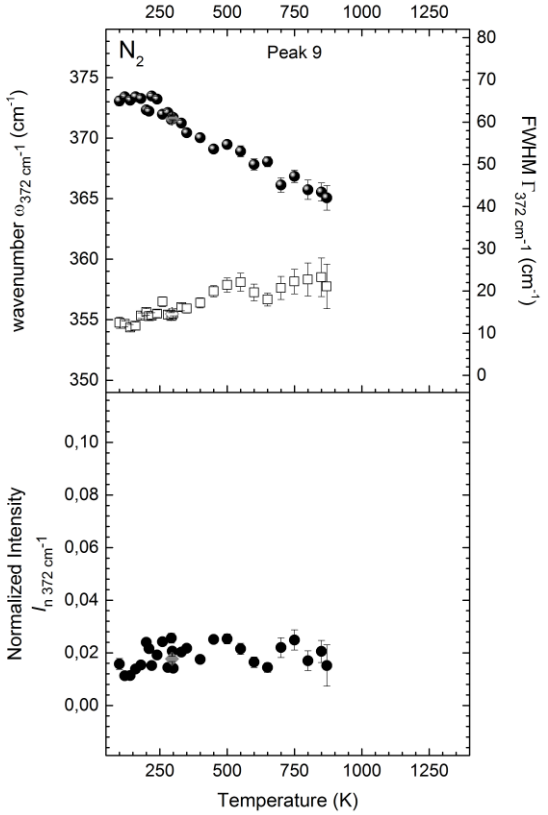
N2
Peak 9
wavenumber ω372 cm-1 (cm-1)
FWHM Γ372 cm-1 (cm-1)
Normalized Intensity
In 372 cm-1
Temperature (K)

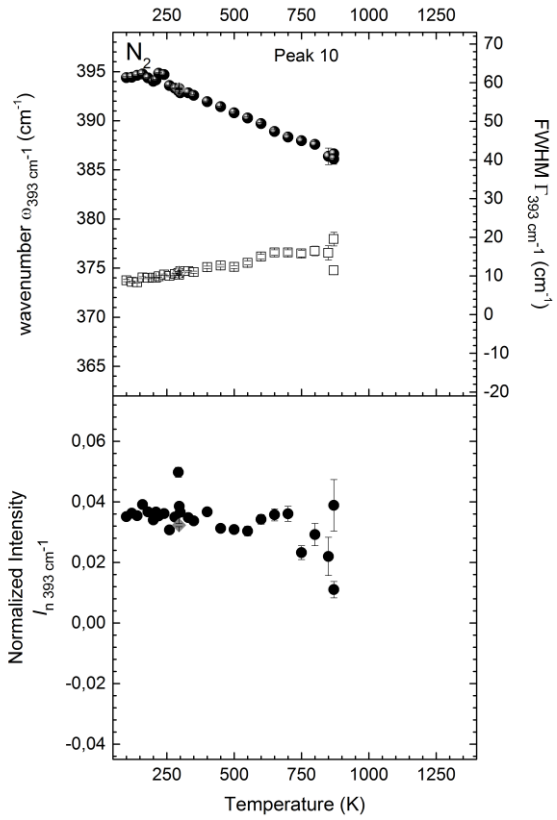
N2
Peak 10
wavenumber ω393 cm-1 (cm-1)
FWHM Γ393 cm-1 (cm-1)
Normalized Intensity
In 393 cm-1
Temperature (K)

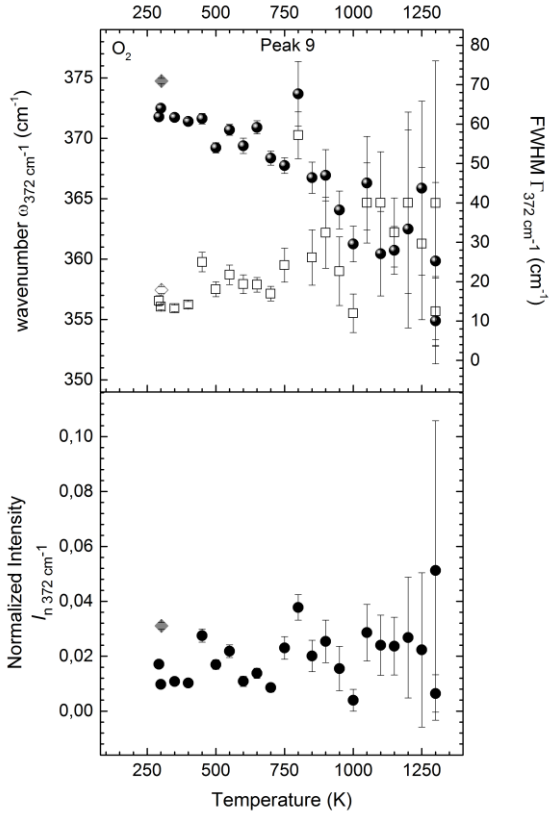
O2
Peak 9
wavenumber ω372 cm-1 (cm-1)
FWHM Γ372 cm-1 (cm-1)
Normalized Intensity
In 372 cm-1
Temperature (K)

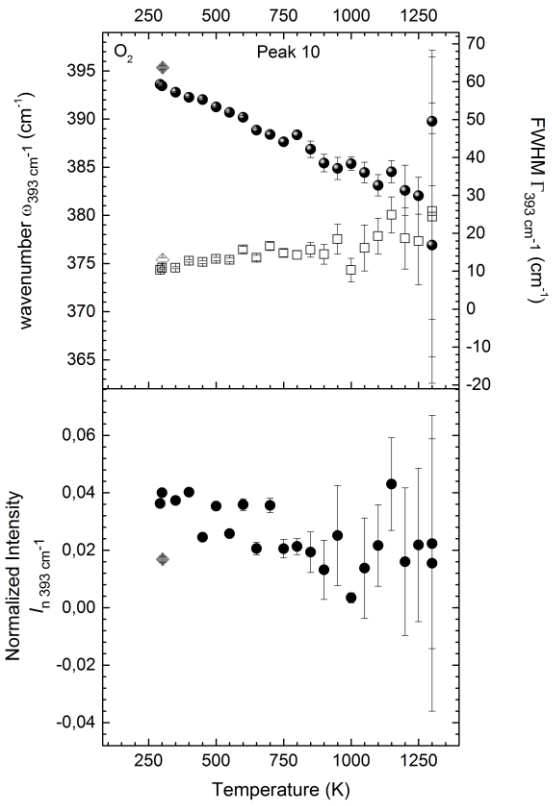
O2
Peak 10
wavenumber ω393 cm-1 (cm-1)
FWHM Γ393 cm-1 (cm-1)
Normalized Intensity
In 393 cm-1
Temperature (K)

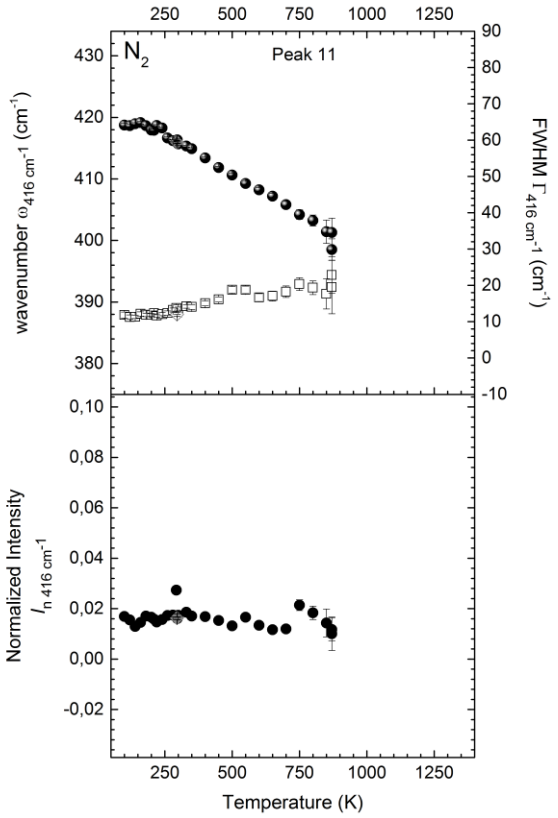
N2
Peak 11
wavenumber ω416 cm-1 (cm-1)
FWHM Γ416 cm-1 (cm-1)
Normalized Intensity
In 416 cm-1
Temperature (K)

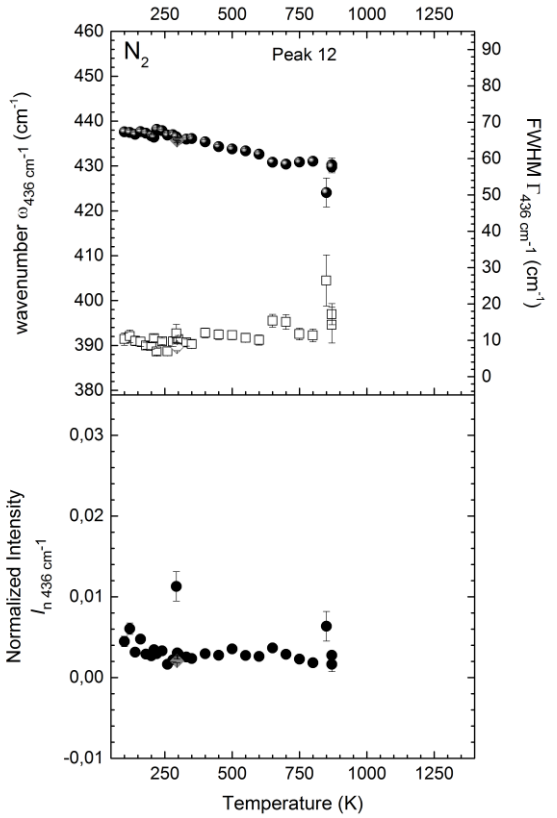
N2
Peak 12
wavenumber ω436 cm-1 (cm-1)
FWHM Γ436 cm-1 (cm-1)
Normalized Intensity
In 436 cm-1
Temperature (K)

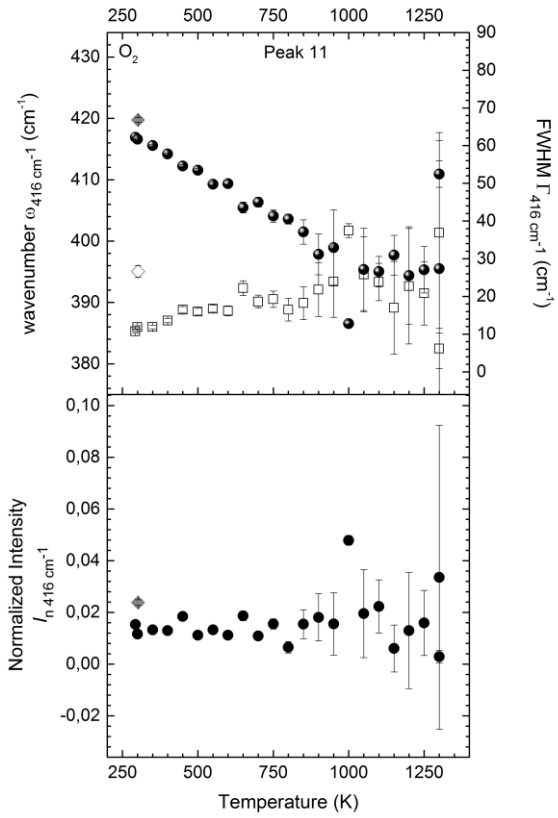
O2
Peak 11
wavenumber ω416 cm-1 (cm-1)
FWHM Γ416 cm-1 (cm-1)
Normalized Intensity
In 416 cm-1
Temperature (K)

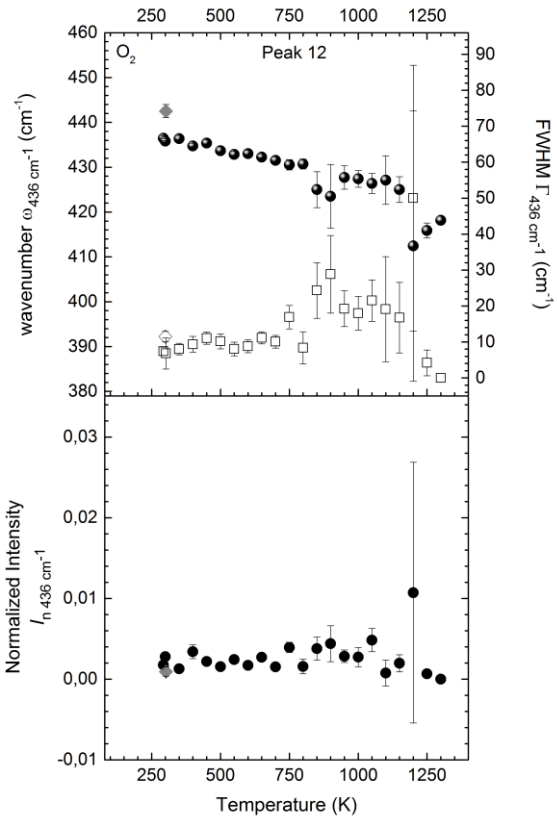
O2
Peak 12
wavenumber ω436 cm-1 (cm-1)
FWHM Γ436 cm-1 (cm-1)
Normalized Intensity
In 436 cm-1
Temperature (K)

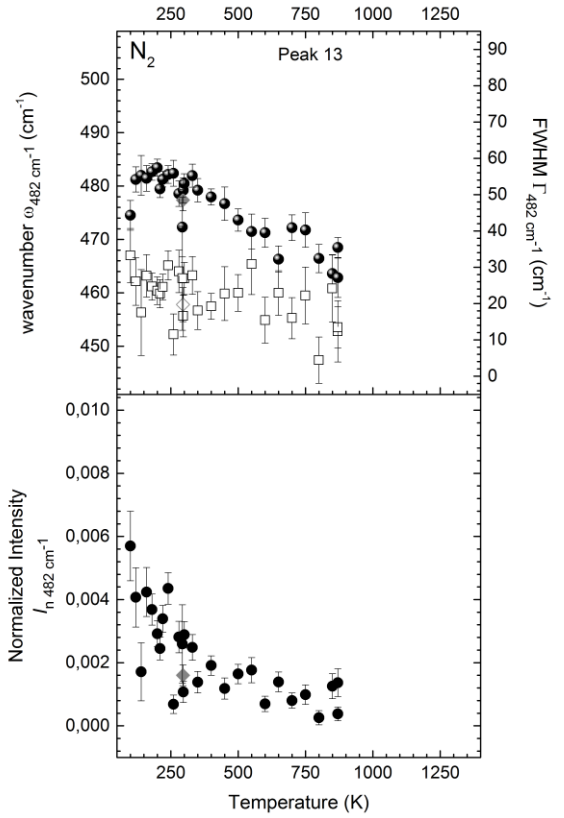
N2
Peak 13
wavenumber ω482 cm-1 (cm-1)
FWHM Γ482 cm-1 (cm-1)
Normalized Intensity
In 482 cm-1
Temperature (K)

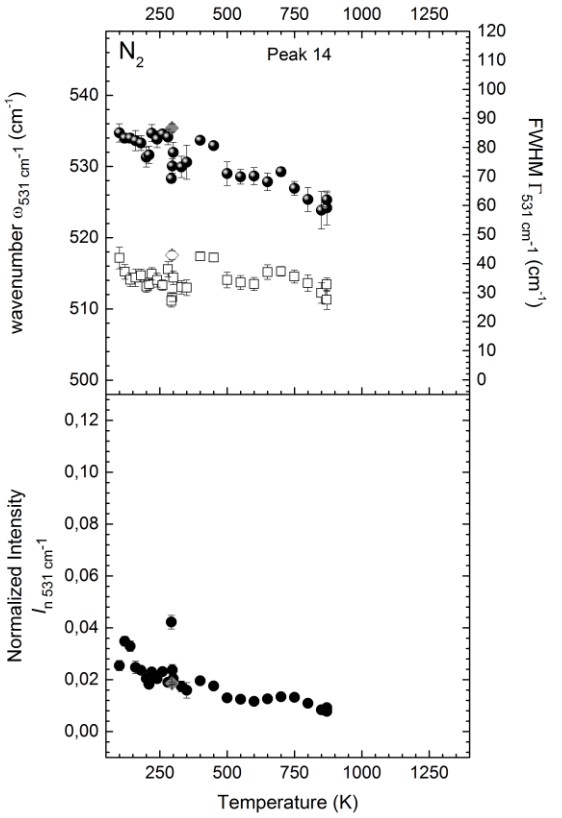
N2
Peak 14
wavenumber ω531 cm-1 (cm-1)
FWHM Γ531 cm-1 (cm-1)
Normalized Intensity
In 531 cm-1
Temperature (K)

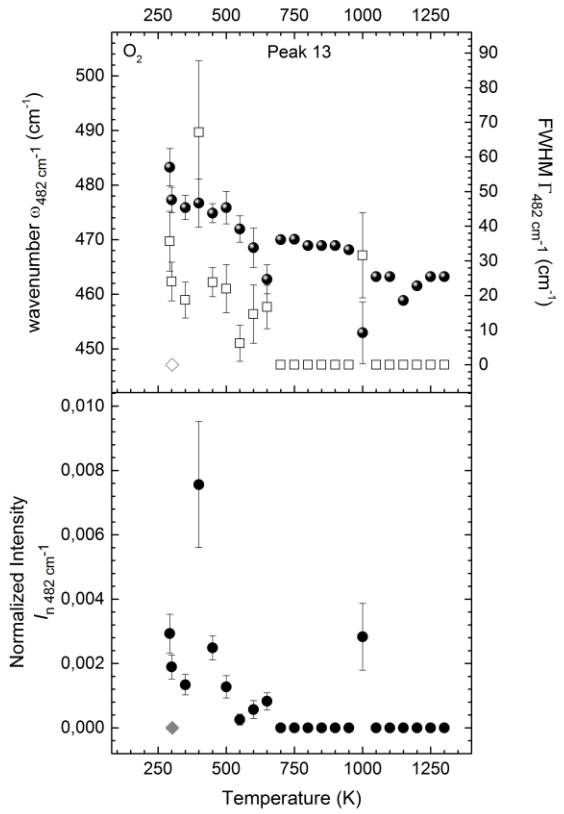
O2
Peak 13
wavenumber ω482 cm-1 (cm-1)
FWHM Γ482 cm-1 (cm-1)
Normalized Intensity
In 482 cm-1
Temperature (K)

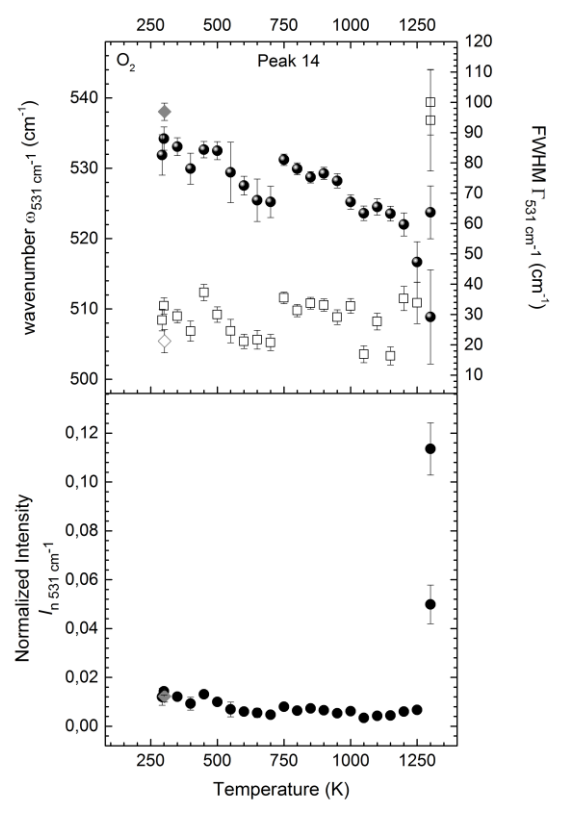
O2
Peak 14
wavenumber ω531 cm-1 (cm-1)
FWHM Γ531 cm-1 (cm-1)
Normalized Intensity
In 531 cm-1
Temperature (K)

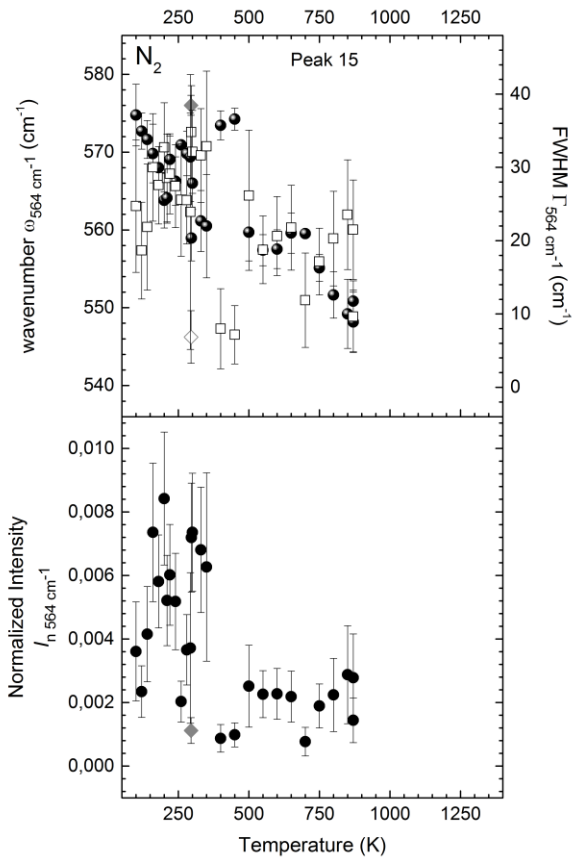
N2
Peak 15
wavenumber ω564 cm-1 (cm-1)
FWHM Γ564 cm-1 (cm-1)
Normalized Intensity
In 564 cm-1
Temperature (K)

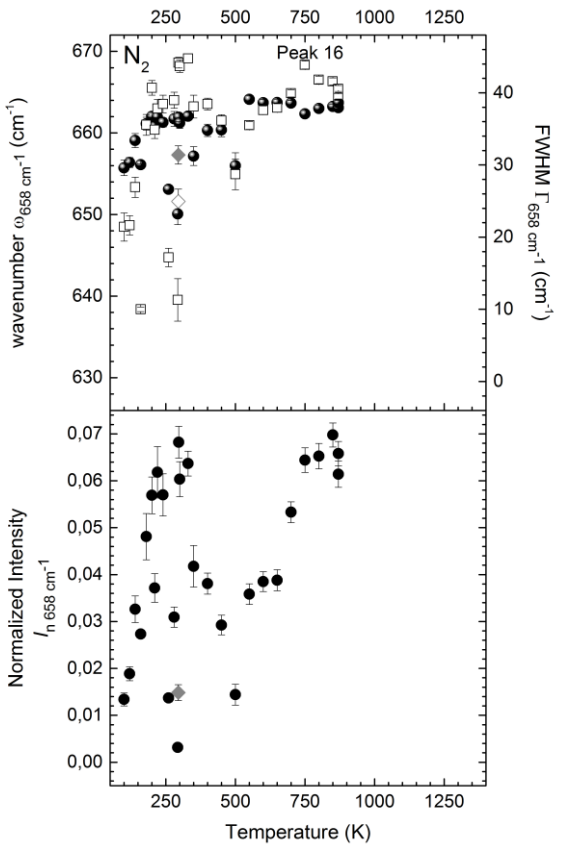
N2
Peak 16
wavenumber ω658 cm-1 (cm-1)
FWHM Γ658 cm-1 (cm-1)
Normalized Intensity
In 658 cm-1
Temperature (K)

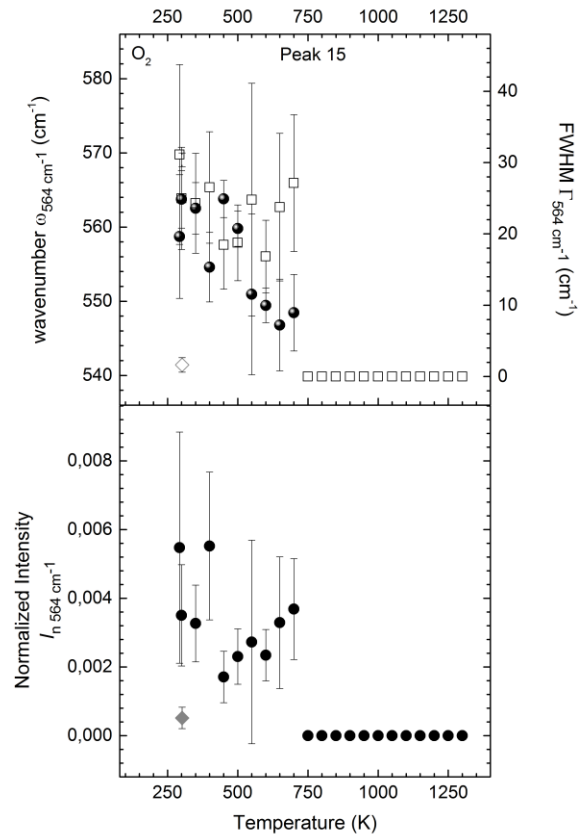
O2
Peak 15
wavenumber ω564 cm-1 (cm-1)
FWHM Γ564 cm-1 (cm-1)
Normalized Intensity
In 564 cm-1
Temperature (K)

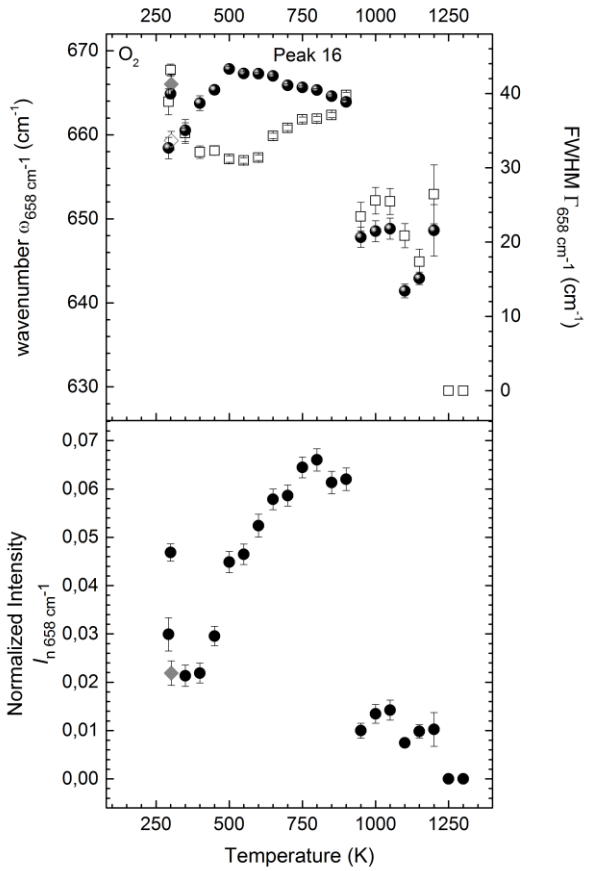
O2
Peak 16
wavenumber ω658 cm-1 (cm-1)
FWHM Γ658 cm-1 (cm-1)
Normalized Intensity
In 658 cm-1
Temperature (K)

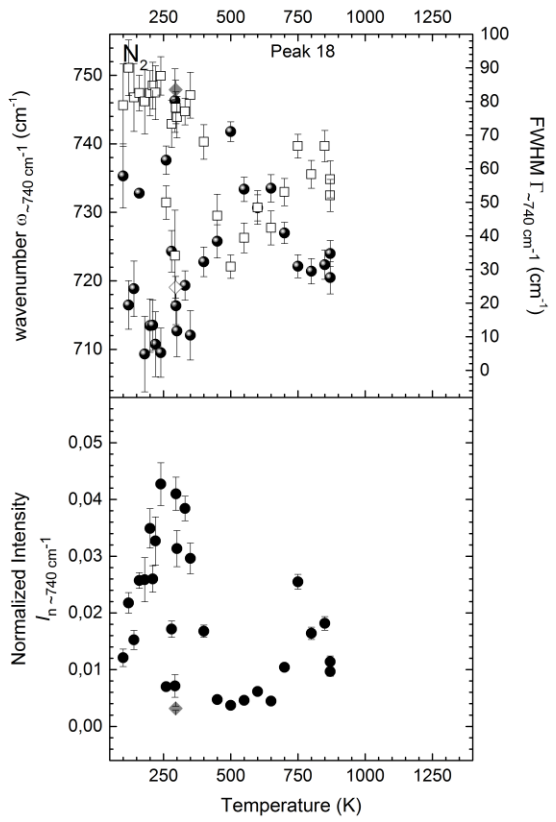
N2
Peak 18
wavenumber ω~740 cm-1 (cm-1)
FWHM Γ~740 cm-1 (cm-1)
Normalized Intensity
In ~740 cm-1
Temperature (K)

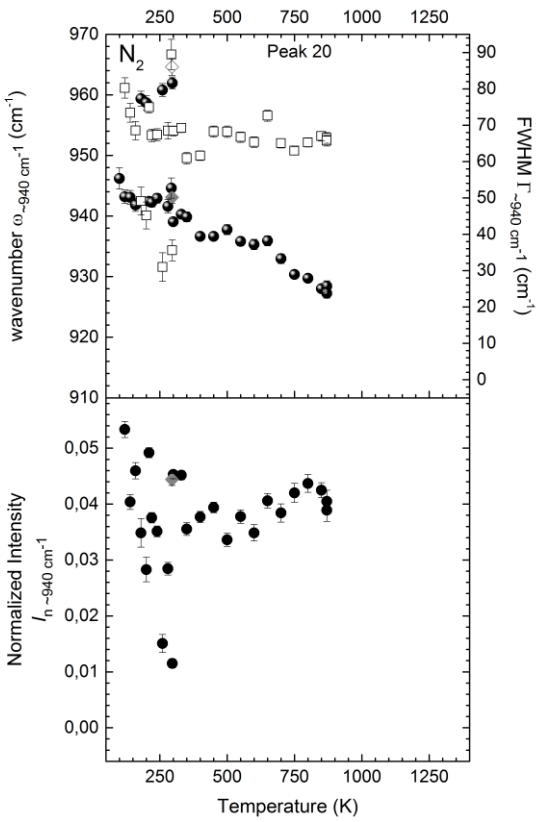
N2
Peak 20
wavenumber ω~940 cm-1 (cm-1)
FWHM Γ~940 cm-1 (cm-1)
Normalized Intensity
In ~940 cm-1
Temperature (K)

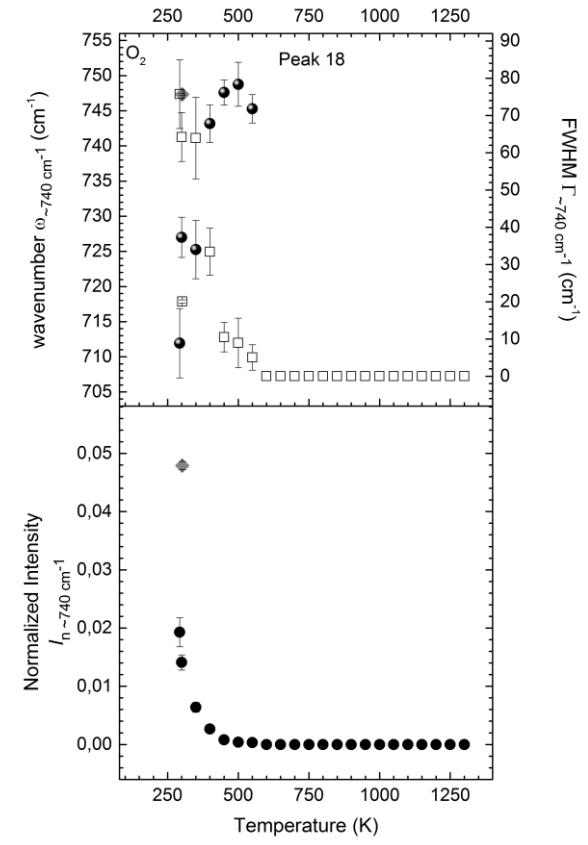
O2
Peak 18
wavenumber ω~740 cm-1 (cm-1)
FWHM Γ~740 cm-1 (cm-1)
Normalized Intensity
In ~740 cm-1
Temperature (K)

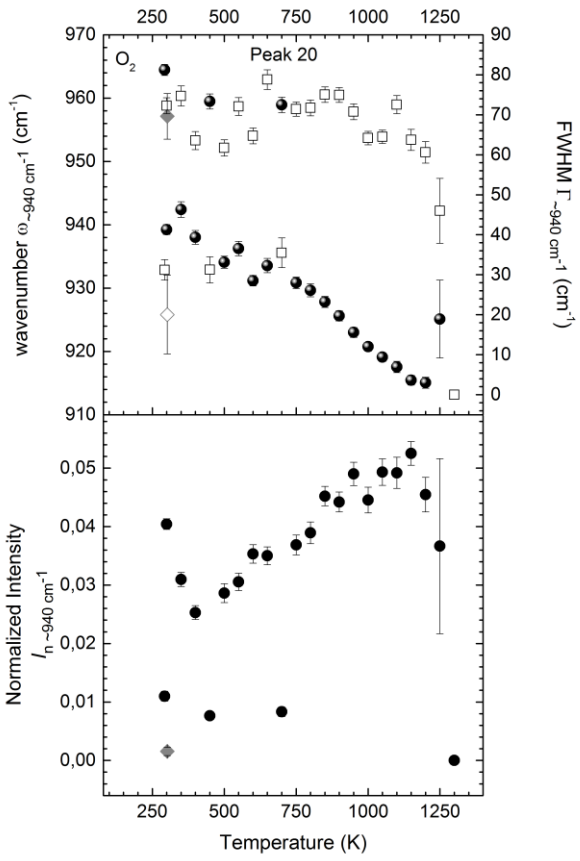
O2
Peak 20
wavenumber ω~940 cm-1 (cm-1)
FWHM Γ~940 cm-1 (cm-1)
Normalized Intensity
In ~940 cm-1
Temperature (K)

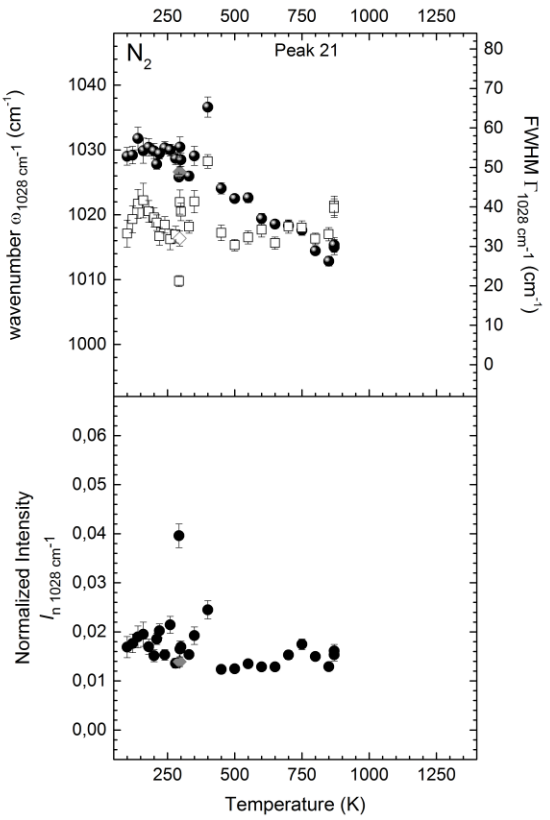
N2
Peak 21
wavenumber ω1028 cm-1 (cm-1)
FWHM Γ1028 cm-1 (cm-1)
Normalized Intensity
In 1028 cm-1
Temperature (K)

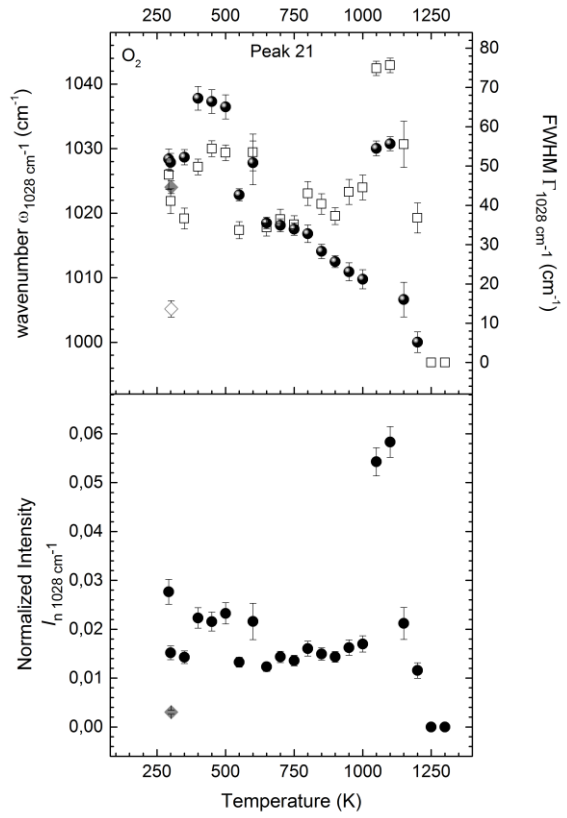
O2
Peak 21
wavenumber ω1028 cm-1 (cm-1)
FWHM Γ1028 cm-1 (cm-1)
Normalized Intensity
In 1028 cm-1
Temperature (K)

Versicherung an Eides statt

Hiermit versichere ich an Eides statt, dass ich die vorliegende Arbeit im Studiengang Geowissenschaften B. Sc. selbstständig verfasst und keine anderen als die angegebenen Hilfsmittel – insbesondere keine im Quellenverzeichnis nicht benannten Internet-Quellen – benutzt habe. Alle Stellen, die wörtlich oder sinngemäß aus Veröffentlichungen entnommen wurden, sind als solche kenntlich gemacht. Ich versichere weiterhin, dass ich die Arbeit vorher nicht in einem anderen Prüfungsverfahren eingereicht habe und die eingereichte schriftliche Fassung der auf dem elektronischen Speichermedium entspricht. Ich bin mit der Ausstellung der Arbeit in der Fachbibliothek einverstanden.

Hamburg, _____ _____